Cell Reports

Article

MOF-mediated PRDX1 acetylation regulates inflammatory macrophage activation

Graphical abstract

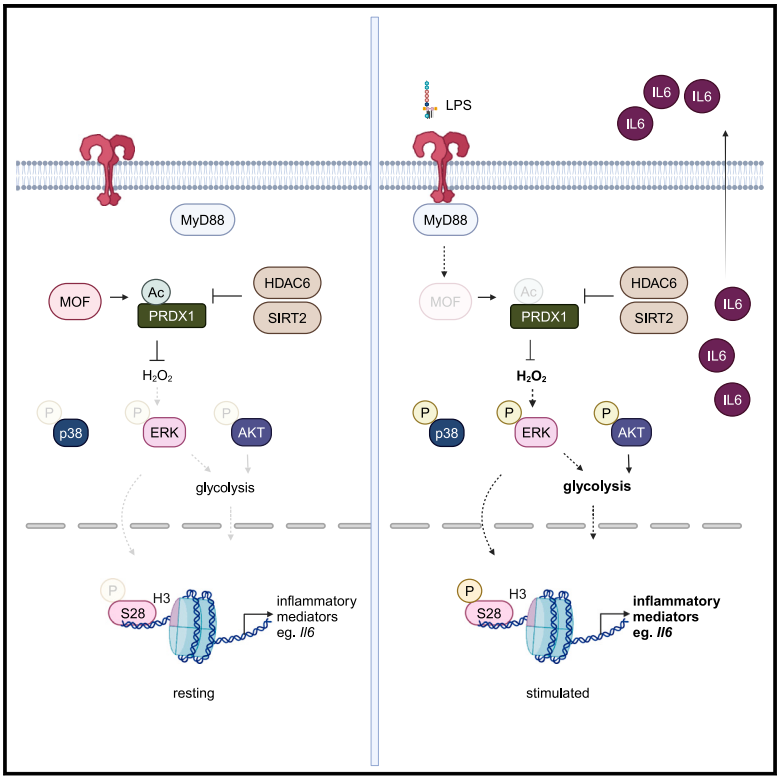

Highlights

- MOF acetylates PRDX1 at lysine 197, which is deacetylated by HDAC6 or SIRT2
- PRDX1 K197 acetylation responds to pro-inflammatory, but not anti-inflammatory, signals
- PRDX1 K197 acetylation regulates cellular hydrogen peroxide accumulation near plasma membrane
- LPS-induced decrease of PRDX1 K197 acetylation augments ERK1/2 phosphorylation

Authors

Hui-Ru Chen, Yidan Sun, Gerhard Mittler, Tobias Rumpf, Maria Shvedunova, Rudolf Grosschedl, Asifa Akhtar

Correspondence

akhtar@ie-freiburg.mpg.de

In brief

Chen et al. demonstrate that MOF regulates LPS-induced macrophage activation via PRDX1 K197 acetylation. Loss of MOF-mediated PRDX1 acetylation increases LPS-induced hydrogen peroxide accumulation, specifically augments ERK1/2 phosphorylation, enhances glycolytic metabolism, and ultimately primes the transcriptional activation of inflammatory genes via H3 S28 phosphorylation.

Chen et al., 2024, Cell Reports *43*, 114682
September 24, 2024
https://doi.org/10.1016/j.celrep.2024.114682

CellPress

Cell Reports

CellPress
OPEN ACCESS

Article

MOF-mediated PRDX1 acetylation regulates inflammatory macrophage activation

Hui-Ru Chen,[1,2] Yidan Sun,[1] Gerhard Mittler,[1] Tobias Rumpf,[1] Maria Shvedunova,[1] Rudolf Grosschedl,[1] and Asifa Akhtar[1,3,*]

[1]Max Planck Institute of Immunobiology and Epigenetics, Freiburg, Baden-Württemberg, Germany
[2]Albert-Ludwigs-University Freiburg, Faculty of Biology, Freiburg, Baden-Württemberg, Germany
[3]Lead contact
*Correspondence: akhtar@ie-freiburg.mpg.de
https://doi.org/10.1016/j.celrep.2024.114682

SUMMARY

Signaling-dependent changes in protein phosphorylation are critical to enable coordination of transcription and metabolism during macrophage activation. However, the role of acetylation in signal transduction during macrophage activation remains obscure. Here, we identify the redox signaling regulator peroxiredoxin 1 (PRDX1) as a substrate of the lysine acetyltransferase MOF. MOF acetylates PRDX1 at lysine 197, preventing hyperoxidation and thus maintaining its activity under stress. PRDX1 K197ac responds to inflammatory signals, decreasing rapidly in mouse macrophages stimulated with bacterial lipopolysaccharides (LPSs) but not with interleukin (IL)-4 or IL-10. The LPS-induced decrease of PRDX1 K197ac elevates cellular hydrogen peroxide accumulation and augments ERK1/2, but not p38 or AKT, phosphorylation. Concomitantly, diminished PRDX1 K197ac stimulates glycolysis, potentiates H3 serine 28 phosphorylation, and ultimately enhances the production of pro-inflammatory mediators such as IL-6. Our work reveals a regulatory role for redox protein acetylation in signal transduction and coordinating metabolic and transcriptional programs during inflammatory macrophage activation.

INTRODUCTION

Inflammation is a tightly controlled immune process responding to various stimuli. Macrophages are sentinel immune cells central to orchestrating inflammation.[1,2] In response to stimuli, naive macrophages undergo metabolic and transcriptional reprogramming to polarize into diverse activated states.[3,4] Pro-inflammatory macrophages are induced by Toll-like receptor (TLR) agonists such as bacterial lipopolysaccharides (LPSs), whereas anti-inflammatory macrophages are generated by helper T (Th) 2 cytokines such as interleukin (IL)-4 or immune suppressors such as IL-10.[5,6] Successful inflammation resolution relies on balancing pro- and anti-inflammatory macrophages at the inflammation site.

Macrophage activation correlates highly with cellular metabolism.[4,7] Inflammatory macrophages predominantly utilize aerobic glycolysis, whereas anti-inflammatory macrophages relatively rely on mitochondrial oxidative phosphorylation. These metabolic adaptations are crucial for determining macrophage functional states.[4,8] Signaling transduction driving macrophage activation impacts metabolic pathways and transcription.[9] In immediate response to LPS, Myd88, and TIR domain-containing adaptor-inducing interferon-β (TRIF) promote glycolytic metabolism in macrophages.[10] In TLR-activated dendritic cells, the TBK/IKKε/AKT (TANK binding kinase/IκB kinase ε/protein kinase B) pathway rapidly stimulates glycolysis to support anabolic demands.[9,11] However, detailed signaling pathways guiding early glycolytic metabolism in inflammatory macrophages remain unexplored.

Peroxiredoxin (PRDX) 1 is a thiol-dependent peroxidase that reduces hydrogen peroxide[12,13] and has been shown to participate in signal transduction, such as mitogen-activated protein kinase (MAPK)[8,14–23] and phosphatase and tensin homolog (PTEN) pathways,[24,25] by modulating intracellular hydrogen peroxide levels. Hydrogen peroxide acts by oxidizing effectors' cysteine and thus regulates the activity of effectors. For example, cysteine oxidation inhibits the activity of phosphatases, such as PTEN,[26,27] whereas it activates the activity of kinases, such as extracellular signal-regulated kinase 1/2 (ERK1/2).[28] Several post-translational modifications (PTMs) have been identified on PRDX1, regulating the peroxidase activity of PRDX1.[29–31] Nevertheless, the function of modified PRDX1 in signal transduction is not well understood. Phosphorylation of PRDX1 at tyrosine 194 suggests a role of PRDX1 in signal transduction. This phosphorylation occurs near the plasma membrane upon growth factor stimulation, inactivating its peroxidase activity and allowing localized hydrogen peroxide accumulation for cysteine oxidation of effectors.[32] While evidence suggests PRDX1's involvement in non-immune cell signal transduction, its function in macrophages responding to physiological hydrogen peroxide production remains unknown.

Males absent on the first (MOF, also known as MYST1 or KAT8) is a lysine acetyltransferase (KAT) that catalyzes histone H4 at lysine 16 (H4K16ac), activating transcription,[33–35] and

plays an important role in cell development, proliferation, cell cycle, and autophagy.[36,37] Besides histone H4, MOF can also acetylate non-histone proteins, modulating their properties and thus participating in various biological processes.[38–45] Although some research has explored the role of MOF in response to specific environmental stimuli and in cellular metabolism maintenance,[40,46,47] its function in macrophages remains largely unknown. Recently, MOF's role in anti-viral immunity was characterized, where it acetylates IRF3, negatively regulating the transcriptional activity of IRF3 and reducing type I interferon production.[40] To investigate the mechanism underpinning the coordination between initial signaling and cellular metabolism during macrophage activation, we looked into our acetylome analysis and found that PRDX1 might be a potential acetylation target of MOF.[44] We aimed to determine if PRDX1 is a MOF substrate and if this acetylation participates in signal transduction and cellular metabolism during macrophage activation.

In this study, we demonstrated that MOF directly acetylates PRDX1 at lysine 197 (PRDX1 K197ac) and this acetylation protects PRDX1 from hyperoxidation, thus maintaining PRDX1's activity under stress conditions. We observed that both MOF and PRDX1 K197ac levels decrease during the early responses in inflammatory macrophages, but not in anti-inflammatory macrophages. PRDX1 K197 acetylation negatively regulates LPS-induced hydrogen peroxide accumulation, ERK1/2 activation, glycolytic metabolism, and IL-6 production. Our findings reveal that acetylation of a redox signaling protein guides early metabolic commitment, supporting transcriptional reprogramming during inflammatory macrophage activation.

RESULTS

MOF acetylates PRDX1 at lysine 197

Our previous MOF acetylome screening identified PRDX1 as a potential MOF target.[44] To verify that PRDX1 is a direct substrate of MOF, we performed *in vitro* histone acetyltransferase (HAT) assays followed by anti-acetyllysine (AcK) antibody immunoblotting. We found that MOF directly acetylates PRDX1 (Figures 1A and S1A).

Mass spectrometry analysis of *in vitro*-acetylated PRDX1 identified lysine 197 as the major acetylation site, with 66% of lysine 197-containing peptides acetylated and 30% of lysine 192-containing peptides acetylated by MOF, while other detected lysine sites were from 0% to 4% acetylated (Figures 1B and S1B). This result suggested that lysine 197 of PRDX1 might be the major acetylation site for MOF. To detect PRDX1 acetylation at lysine 197, we generated an antibody against K197 acetylation of PRDX1 (PRDX1 K197ac). The specificity of the PRDX1 K197ac antibody was confirmed by three findings. First, *in vitro* HAT assay followed by immunoblotting with the PRDX1 K197ac antibody showed that MOF acetylated PRDX1 at K197 in a dose-dependent manner (Figure 1C). Second, we mutated lysine 197 and lysine 192, the two most abundant acetylated sites identified in our mass spectrometry analysis (Figure 1B), as well as three other lysine residues (K7, K109, 136) that scored in previous MOF acetylome screening,[44] one at a time. The five lysine residues are highly conserved in mammals and accessible on the surface of PRDX1 (Figures 1D and S1C). Mutating a lysine to arginine (K-R) generates a residue that resists acetylation while maintaining the positive charge. The results showed that mutating lysine 197 abolished site-specific acetylation of PRDX1 at K197 and dramatically reduced overall PRDX1 acetylation levels, while mutations at other lysines did not affect K197 acetylation (Figure 1E), confirming that K197 is the major acetylation site for MOF and PRDX1 K197ac antibody is indeed specific to K197 acetylation of PRDX1. Importantly, the PRDX1 K197ac antibody did not recognize non-acetylated purified PRDX1 (Figure 1C, lane 1, and Figure 1E, lane 1–3). Third, immunoblotting analysis of *Prdx1* knockout (KO) Raw264.7 macrophages (Figure S1D) showed an absence of signal from the PRDX1 K197ac antibody in both steady state and LPS-stimulated *Prdx1* KO cells (Figures S1E and S1F), suggesting the PRDX1 K197ac antibody does not cross-react with other PRDX family proteins in cells. Notably, the peroxidase-defective peroxidatic (Cys 52) and resolving cysteine (Cys 173) double mutant (2CS) exhibited lower PRDX1 K197ac levels (Figure 1E, lane 10), implying that the cysteine resides at positions 52 and 173 boost K197 acetylation. Furthermore, coenzyme A (CoA) decreased PRDX1 K197 acetylation in the HAT assay, emphasizing that MOF enzymatically acetylates PRDX1 (Figure S1G).

We investigated the contribution of MOF in acetylating PRDX1 at lysine 197 by knocking down MOF in mouse bone-marrow-derived macrophages (BMDMs) (Figures S1H and S1I) and human HEK293 cells. MOF depletion decreased PRDX1 K197ac, indicating MOF mediates this acetylation in macrophages (Figure 1F) and in a cancer cell line (Figure 1G). Although PRDX1 is known to be deacetylated by HDAC6 or SIRT2 in cancer cells,[29,30] the deacetylation sites targeted by these enzymes have not been identified and it remains unclear whether deacetylation also occurs in macrophages. BMDMs treated with a specific HDAC6 inhibitor tubacin (Figure 1H) or depleted of SIRT2 (Figure 1I) showed increased PRDX1 K197ac, suggesting HDAC6 and SIRT2 reversibly modify PRDX1 K197 acetylation in macrophages.

MOF protein and K197 acetylation of PRDX1 levels decrease in immediate response to LPS but not to IL-4 or IL-10

To explore the role of PRDX1 K197ac during macrophage activation, we stimulated BMDMs with LPS for inflammatory response and with IL-4 or IL-10 for anti-inflammatory response (Figure 2A). We observed that PRDX1 K197ac levels and MOF protein levels were both decreased following LPS stimulation (Figures 2B–2E), while they were not affected following stimulation with IL-4 (Figures 2F–2I) or IL-10 (Figures 2J–2M), implying a specific role of MOF-mediated K197 acetylation of PRDX1 in LPS-induced inflammatory macrophages. *Myd88*-deficient or *Trif*-depleted BMDMs stimulated with LPS showed no reduction in PRDX1 K197ac or MOF levels, indicating the necessity of Myd88 and TRIF pathways (Figures S2A–S2E). Since PRDX1 has been detected in cytosol, plasma membrane, nucleus, and chromatin.,[32,48–50] we asked which subcellular PRDX1 K197ac pool contributes to the response to LPS. Our subcellular fractionation result revealed that the LPS-induced decrease in PRDX1 K197 acetylation levels occurred in the cytoplasmic and membrane fractions (Figures S2F and S2G), consistent with studies focusing on the role of PRDX1 in signaling

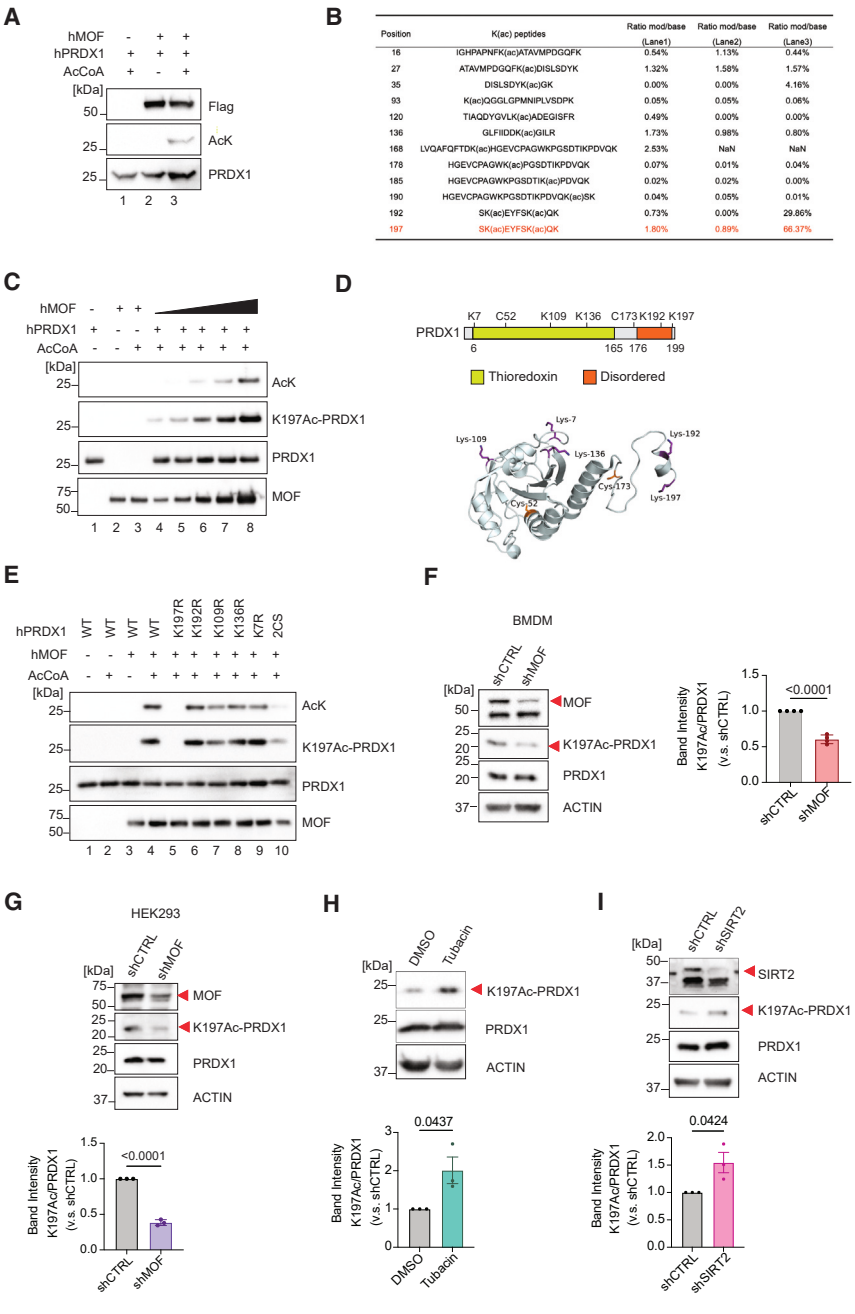

Figure 1. MOF acetylates PRDX1 at lysine 197

(A) *In vitro* HAT assay with FLAG-tagged human MOF (hMOF) proteins on recombinant human PRDX1 (hPRDX1) protein (lane 3) followed by western blot for acetyllysine (AcK), PRDX1, and FLAG (MOF). Negative controls: without hMOF (lane 1) or AcCoA (lane 2).

(B) Mass spectrometry analysis from the *in vitro* HAT assay. Lane 1, without MOF; lane 2, without AcCoA; lane 3, presence of MOF, PRDX1, and AcCoA ($n = 3$).

(C) *In vitro* HAT assays with increasing concentrations of hMOF protein (0.1, 0.2, 0.5, 1, 2 μM) on hPRDX1 protein followed by western blot for AcK, PRDX1 K197ac, PRDX1, and MOF. Negative controls in lanes 1–3.

(D) Protein domain and indicated lysine sites (Lys7, Lys109, Lys136, Lys192, Lys197), peroxidatic (Cys52), and resolving (Cys173) cysteines on human PRDX1. Protein structure illustration created by Pymol using PDB: 2X9S.

(E) *In vitro* HAT assays with hMOF on WT, lysine-to-arginine mutants of hPRDX1 (K197R, K192R, K109R, K136R, K7R), or cysteine-to-serine double mutant (2CS, C52S/C173S).

(F–I) Western blot analysis of PRDX1 K197ac in MOF-depleted (shMOF) mouse BMDM (F), HEK293 human cells (G), BMDMs treated with 16 μM tubacin for 18 h (H), or BMDMs depleted of SIRT2 (shSIRT2) (I). shCTRL: shRNA control harboring non-targeting sequence for mammalian cells. Band intensities from three or four experiments were quantified, and relative levels of K197ac/total PRDX1 normalized to control were analyzed with a two-tailed unpaired t test. Data shown as mean ± SEM (F and G).

transduction.[21,23,51] In fact, our fractionation result showed a small portion of MOF in the cytoplasm (Figure S2J). Conversely, PRDX1 K197ac levels in soluble nuclear and chromatin fractions corresponded to bulk PRDX1 protein levels (Figures S2H and S2I), implying that the regulation of PRDX1 K197ac is unlikely to occur in the nucleus.

LPS-induced decrease of PRDX1 K197 acetylation elevates cellular hydrogen peroxide accumulation

To determine the functional alteration elicited by K197 acetylation, we evaluated its effect on peroxidase activity using a lysine to glutamine (K-Q) mutant, mimicking acetylation, and performing *in vitro* peroxidase assays[52] (Figures 3A and S3A). The results showed that, at the onset of the reaction, there was no significant difference in NADPH oxidation between the wild type (WT) (Figure 3B, blue line) and K197Q mutant (Figure 3B, purple line). However, after approximately 800 s (13 min) of incubation, the NADPH oxidation in the K197Q mutant began to surpass that of the WT protein. This suggested that K197 acetylation of PRDX1 could enhance its peroxidase activity upon prolonged exposure to hydrogen peroxide.

During the catalytic cycle, PRDX1 is oxidized by hydrogen peroxide, forming homodimers. These homodimers are further reduced by the thioredoxin (Trx)/Trx reductase (TrxR) system to monomers for the next catalytic cycle. Under persistent or high concentrations of hydrogen peroxide exposure, PRDX1 undergoes hyperoxidation, where PRDX1 is further oxidized to a monomeric hyperoxidized form that cannot be reduced by the Trx/TrxR system (Figures S3B).[25,53] Therefore, to investigate how K197 acetylation enhances the peroxidase activity of

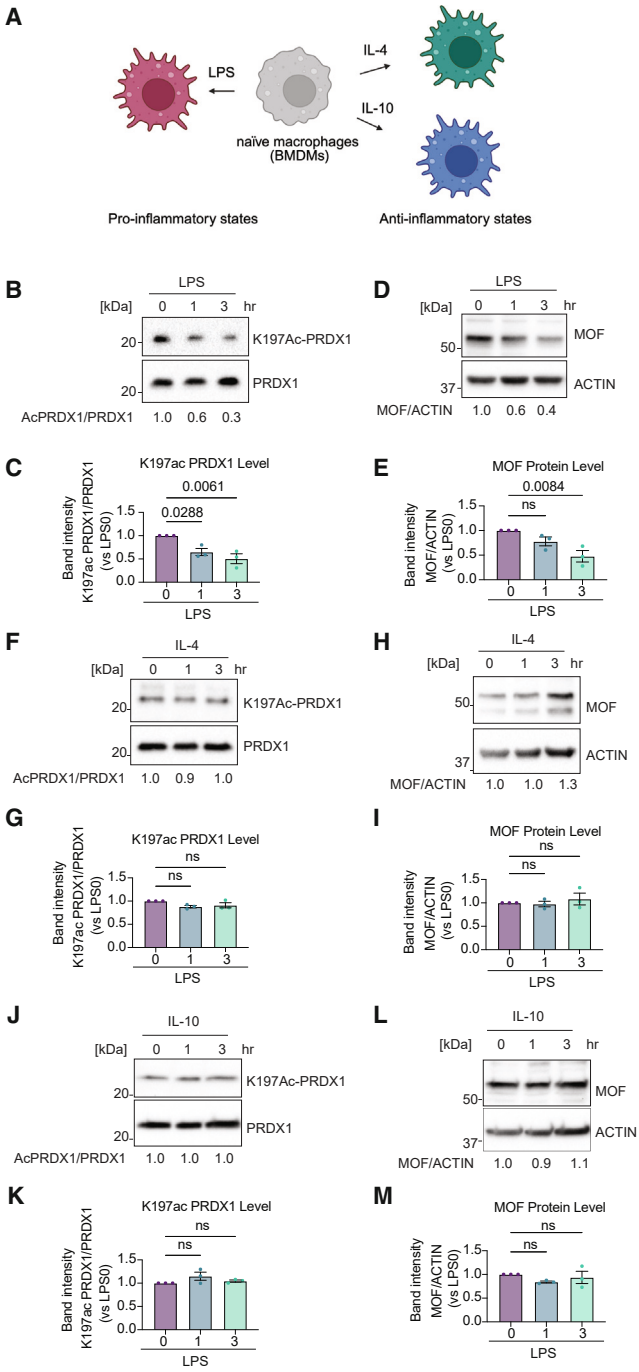

Figure 2. MOF protein and K197 acetylation of PRDX1 levels decrease in immediate response to LPS but not to IL-4 or IL-10

(A) Schematic illustration of pro-inflammatory and anti-inflammatory macrophage activation.

(B–E) Western blot time course analysis of PRDX1 K197ac (B) and MOF (D) in BMDMs in response to LPS (100 ng/mL) at indicated time points (hours).

(F–I) Western blot time course analysis of PRDX1 K197ac (F) and MOF (H) in BMDMs in response to IL-4 (20 ng/mL) at indicated time points (hours).

(J–M) Western blot time course analysis of PRDX1 K197ac (J) and MOF (L) in BMDMs in response to IL-10 (10 ng/mL) at indicated time points (hours). Band intensities from three experiments were quantified, and relative levels of K197ac/total PRDX1 or MOF/ACTIN normalized to control were analyzed with one-way ANOVA followed by Dunnett's multiple comparison test. Data shown as mean ± SEM (C, E, G, I, K, M).

PRDX1, we examined the redox state of PRDX1 K197ac in *Prdx1* KO HEK293 cells complemented with either empty vector (EV), FLAG-tagged WT, K197R, or K197Q PRDX1 (Figures S3C and S3D). In the steady state, K197Q mutant showed an increased proportion of monomeric PRDX1 compared to WT or K197R mutant (Figures S3E and S3H). A 10-min exposure to hydrogen peroxide resulted in an increased proportion of dimeric PRDX1 where the K197 mutations did not significantly impact the monomer-to-dimer ratio compared to WT (Figures S3E and S3F). This observation supported the finding that the K197Q mutant has similar peroxidase activity to WT in the *in vitro* peroxidase assay within 13 min of incubation. Importantly, K197Q mutant exhibited a lower level of PRDX1 hyperoxidation upon 10-min exposure to hydrogen peroxide (Figures S3G). Prolonged exposure to hydrogen peroxide (3 h) resulted in an increased proportion of monomeric PRDX1, particularly in K197Q mutant (Figure S3H and S3I). Similar to 10-min exposure, persistent hydrogen peroxide exposure for 3 h maintained a lower level of hyperoxidation in K197Q mutant compared to K197R mutant (Figure S3J). These results suggest that K197-acetylated PRDX1 possesses higher resistance to hyperoxidation, which could potentially contribute to the observed elevation in peroxidase activity resulting from acetylation at lysine 197 of PRDX1. Together, K197 acetylation impacts the kinetics of peroxidase activity, particularly under prolonged hydrogen peroxide exposure: at the onset of the cycle, the peroxidase activity of constitutively acetylated PRDX1 is comparable to WT but surpasses WT by lowering its hyperoxidation level.

We sought to investigate whether the regulation of PRDX1 peroxidase activity by K197 acetylation modulates cellular hydrogen peroxide levels in response to LPS in macrophages. Peroxy Orange 1 staining in BMDMs showed that loss of MOF increased cellular hydrogen peroxide accumulation following 3-h LPS stimulation but did not affect cellular hydrogen peroxide accumulation in unstimulated macrophages (Figure 3C), suggesting an LPS-dependent role for MOF in regulating the redox state of macrophages. RNA sequencing showed that transcript levels of reactive oxygen species (ROS)-metabolizing and redox-regulating enzymes, including PRDX1 (Figure 3D), were unchanged in both LPS-stimulated and unstimulated MOF-depleted BMDMs (Figure 3E), indicating LPS-induced MOF-dependent hydrogen peroxide accumulation is likely to be a post-transcriptional event.

Prdx1 KO in Raw264.7 cells increased hydrogen peroxide accumulation when unstimulated; LPS stimulation for 3 h further enhanced this accumulation (Figure 3F), highlighting the role of PRDX1 in scavenging hydrogen peroxide in macrophages. To assess the hydrogen peroxide-scavenging capacity of K197-acetylated PRDX1, we used *Prdx1* KO Raw264.7 cells for complementation assays with either EV, FLAG-tagged WT, K197R, or K197Q PRDX1 (Figure 3G). In unstimulated conditions, WT or K197Q PRDX1, but not K197R or 2CS PRDX1 mutants, rescued elevated hydrogen peroxide levels caused by loss of PRDX1

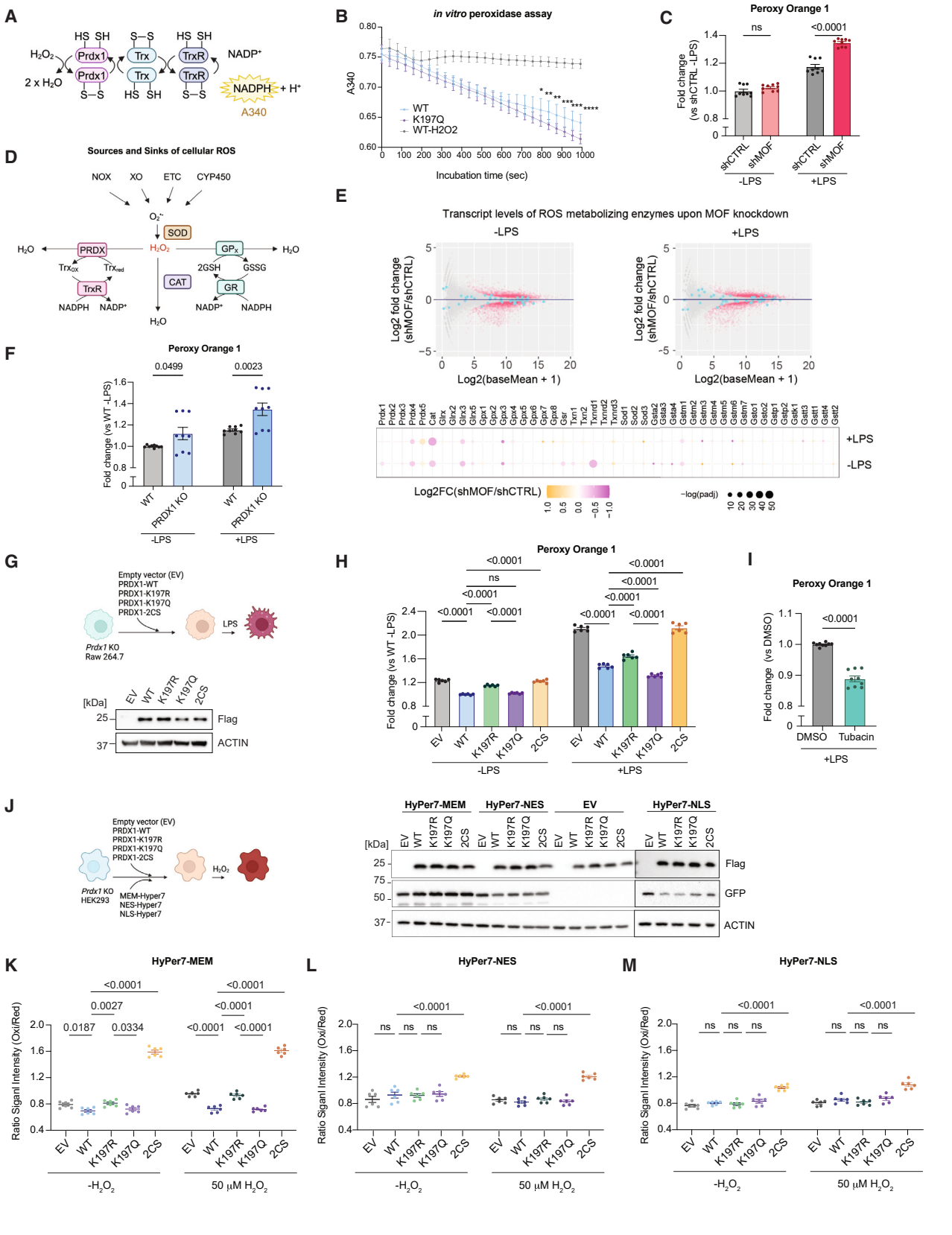

(legend on next page)

(Figure 3H). Three-hour-LPS-stimulated *Prdx1* KO cells complemented with EV, K197R, or 2CS mutant had higher hydrogen peroxide levels than those with WT PRDX1. K197Q mutant cells showed lower hydrogen peroxide levels than WT PRDX1 (Figure 3H), consistent with *in vitro* peroxidase assays showing the acetylation at lysine 197 on PRDX1 enhances its peroxidase activity upon prolonged exposure to hydrogen peroxide (Figure 3B).

Given K197 de-acetylation of PRDX1 is mediated by HDAC6 and SIRT2 (Figures 1H and 1I), we tested their effects on hydrogen peroxide levels in LPS-stimulated macrophages. HDAC6 inhibition by tubacin (Figure 3I) or SIRT2 knockdown (Figure S3K) attenuated LPS-induced hydrogen peroxide accumulation. Collectively, we showed that MOF-mediated PRDX1 K197ac enhances its peroxidase activity, which in turn enables macrophages to restrict hydrogen peroxide accumulation, while HDAC6- or SIRT2-mediated K197 deacetylation of PRDX1 decreases hydrogen peroxide accumulation in response to LPS.

To investigate which subcellular hydrogen peroxide pool is affected by PRDX1 K197ac, we used HyPer7, a pH-insensitive hydrogen peroxide sensor,[54] in *Prdx1* KO HEK293 cells complemented with PRDX1 K197 mutants to examine hydrogen peroxide levels in different compartments (plasma membrane [MEM], cytoplasm [NES], nucleus [NLS]) (Figures 3J–3M and S3L). Cells lacking PRDX1 (EV) showed higher HyPer7-MEM responses at steady state and upon hydrogen peroxide challenge compared to WT PRDX1, indicating the role of PRDX1 in modulating hydrogen peroxide levels in the plasma membrane compartment (Figure 3K). WT and K197Q, but not K197R, PRDX1 reduced HyPer7-MEM responses (Figure 3K), suggesting PRDX1 K197ac regulates hydrogen peroxide levels near the plasma membrane. This was consistent with intracellular hydrogen peroxide staining in BMDMs (Figure 3H). PRDX1 or PRDX1 K197ac had minimal effect on HyPer7 oxidation in cytoplasm and nucleus (Figures 3L and 3M), indicating these compartments may relatively rely on other antioxidants, such as PRDX2.[55] Intriguingly, 2CS mutant PRDX1 showed higher Hyper7 responses compared to *Prdx1* KO cells (EV) in all compartments (Figures 3K–3M), suggesting possible additional functions of the 2CS mutant. Together, our findings indicate that PRDX1 K197ac modulates hydrogen peroxide levels in the vicinity of the plasma membrane. This observation is supported by subcellular fractionation results showing reduced cytoplasmic and membrane-associated PRDX1 K197ac levels upon LPS challenge (Figure S2F–S2I).

LPS-induced reduction of PRDX1 K197 acetylation augments ERK1/2 phosphorylation

Our hydrogen peroxide staining suggested a redox role of MOF in macrophages is LPS dependent (Figure 3C). To systemically investigate the role of MOF upon LPS stimulation, we analyzed differentially expressed genes (DEGs) in MOF-depleted BMDMs: 2,447 upregulated and 2,576 downregulated in unstimulated (−LPS) (Figure 4A; Table S1); 2,286 upregulated and 1,792 downregulated in LPS stimulated (+LPS, 3 h) conditions (Figures 4B; Table S2). We categorized DEGs into six clusters based on LPS response (Figures 4C and 4D). Cluster 1 (1,278 DEGs) and cluster 3 (1,298 DEGs) were downregulated by loss of MOF, unaffected by LPS (Figure 4E). Gene Ontology (GO) analysis showed enrichment in "DNA repair," "DNA replication," "cell cycle phase transition," and "mitosis-related events" (Figure S4A). Cluster 2 (494 DEGs) was downregulated by loss of MOF only with LPS, with no significant enriched GO terms. Cluster 4 (1,073 DEGs) was upregulated by loss of MOF with LPS independence (Figure 4F), showing GO terms "autophagy" and "response to nutrient level" (Figure S4B). Cluster 5 (912 DEGs) was upregulated by LPS and further increased by loss of MOF, enriched in signaling pathways such as "pattern recognition receptor signaling," "immune response-regulating signaling,"

Figure 3. LPS-induced decrease of PRDX1 K197 acetylation elevates cellular hydrogen peroxide accumulation

(A) Schematic illustration of *in vitro* peroxidase assay (Trx, thioredoxin; TrxR, thioredoxin reductase).

(B) *In vitro* peroxidase assay using purified 0.5 μM WT or K197Q mutant of hPRDX1, 5 μM yTrx, 0.5 μM yTrxR, 10 μM hydrogen peroxide, and 200 μM NADPH. Peroxidase activity was monitored by A340 decrease, which reflects NADPH oxidation. Negative controls lack hydrogen peroxide. Data from nine replicates shown as mean ± SEM analyzed with two-way ANOVA followed by Sidak's multiple comparison test. $^{*}p \leq 0.05$, $^{**}p \leq 0.01$, $^{***}p \leq 0.001$, $^{****}p \leq 0.0001$.

(C) Cellular hydrogen peroxide accumulation in MOF-depleted BMDMs stimulated with LPS (100 ng/mL, 3 h) or unstimulated, assessed by Peroxy Orange 1 (PO-1) staining.

(D) Schematic illustration of major hydrogen peroxide-metabolizing enzymes in mammalian cells.

(E) MA plot (the log2 fold changes on the y axis versus the log2 average expression level signal on the x axis) of hydrogen peroxide-metabolizing enzymes in RNA sequencing (RNA-seq) of MOF-depleted BMDMs stimulated with LPS (100 ng/mL, 3 h) or unstimulated. Red dots, DEGs; green dots, hydrogen peroxide-metabolizing enzymes. Log2 fold change (log2FC) (shMOF/shCTRL) and –log(adjusted *p*) of green dots in MA plot are shown in the dot plot.

(F) Cellular hydrogen peroxide accumulation in WT or *Prdx1* KO Raw264.7 cells stimulated with LPS (100 ng/mL, 3 h) or unstimulated, assessed by PO-1 staining.

(G) Schematic illustration of complementation assay in *Prdx1* KO Raw264.7 cells. Western blot shows exogenous WT and mutant PRDX1 protein levels.

(H) Cellular hydrogen peroxide accumulation in *Prdx1* KO Raw264.7 cells complemented with empty vector (EV) or WT, K197R, K197Q, or 2CS mutant PRDX1 stimulated with LPS (100 ng/mL, 3 h) or unstimulated, assessed by PO-1 staining.

(I) Cellular hydrogen peroxide accumulation in BMDMs pre-treated with 16 μM tubacin for 18 h followed by LPS stimulation (100 ng/mL, 3 h) assessed by PO-1 staining.

(J) Schematic illustration of Hyper7 experiments in *Prdx1* KO HEK293 cells. Western blot shows exogenous WT and mutant PRDX1 and Hyper7 levels.

(K–M) Response of plasma membrane-targeted (MEM) (K), cytoplasm-targeted (NES) (L), and nucleus-targeted (NLS) (M) Hyper7 in *Prdx1* KO HEK293 cells complemented with EV, WT, K197R, K197Q, or 2CS PRDX1 treated with 50 μM hydrogen peroxide or untreated. Ratio of oxidized to reduced Hyper7 signals shown as geometric mean ± SEM ($n = 6$, two independent samples in triplicates), analyzed with two-way ANOVA by Tukey's multiple comparisons test.

Fold changes of PO-1 staining in treated samples normalized to control. $n = 9$, three independent samples in triplicates (C, F, and I). $n = 6$, two independent samples in triplicates (H). Data shown as mean ± SEM, analyzed with either two-way ANOVA followed by uncorrected Fisher's least significant difference (LSD) test (C and F), Sidak's multiple comparison test (H), or analyzed with a two-tailed unpaired t test (I).

CellPress
OPEN ACCESS

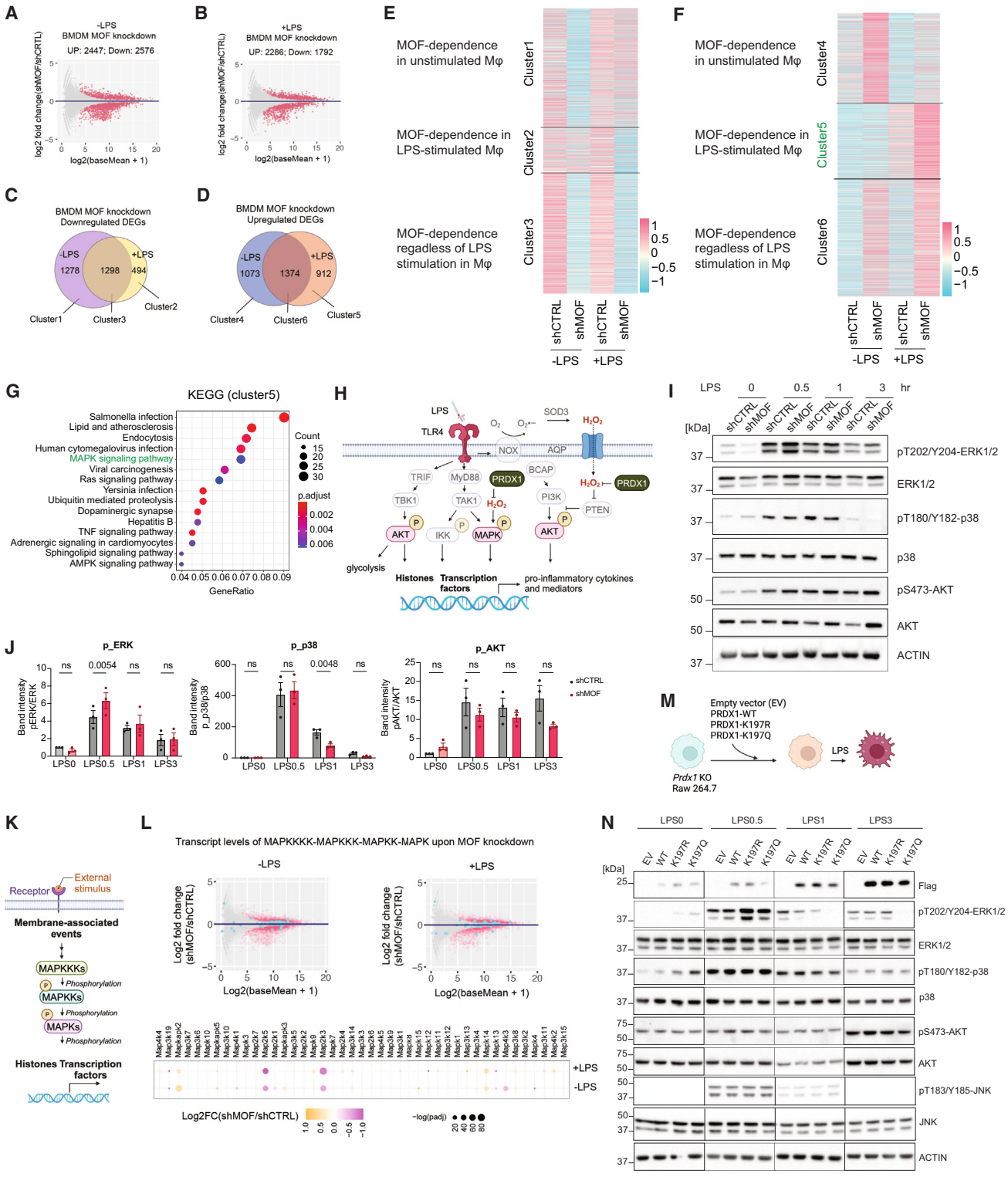

Figure 4. LPS-induced reduction of PRDX1 K197 acetylation augments ERK1/2 phosphorylation

(A and B) MA plot of DEGs (red dots) from RNA-seq in MOF-depleted BMDMs (shMOF vs. shCTRL) stimulated with LPS (100 ng/mL, 3 h) or unstimulated.

(C and D) Venn diagram of DEGs between LPS-stimulated and unstimulated macrophages showing downregulated (C) or upregulated (D) genes.

(E and F) Heatmap of DEGs in each cluster. Cluster 5 (in green) is LPS responsive and MOF sensitive.

(G) GO enrichment analysis for genes in cluster 5 using KEGG in ClusterProfile. MAPK pathway (in green) is enriched.

(legend continued on next page)

"positive regulation of response to external stimulus," and "small GTPase-mediated signal transduction" (Figure S4B), suggesting an unexplored role of MOF in regulating signaling transduction in BMDMs. Moreover, MAPK signaling was the most highly enriched pathways in Kyoto Encyclopedia of Genes and Genomes (KEGG) pathway analysis (Figure 4G). Cluster 6 (1,374 DEGs) was upregulated regardless of LPS, enriched in "T cell activation," "positive regulation of cytokine production," and "regulation of tumor necrosis factor production," and it shared overlapping GO terms with cluster 5, indicating the importance of MOF in macrophage biology (Figure S4B).

RNA sequencing indicates a role for MOF in the MAPK signaling pathway (Figure 4G). Since PRDX1 modulates MAPK and PTEN/PI3K/AKT pathways via regulating cellular ROS levels,[23–25,32,51,56–60] we investigated the effects of MOF-mediated PRDX1 K197ac on MAPK and AKT activation in LPS-induced macrophages (Figure 4H). MOF-depleted BMDMs showed increased ERK1/2 phosphorylation at Thr202/Tyr204 after 30 min of LPS stimulation, without affecting p38 or AKT phosphorylation (Figures 4I and 4J). Transcript levels of MAPK family kinases were not significantly upregulated upon loss of MOF (Figures 4K and 4L). In addition, N-acetylcysteine (NAC) treatment, which reduces cellular ROS levels, attenuated LPS-induced ERK1/2 phosphorylation in MOF-depleted BMDMs (Figure S4C), highlighting the role of ROS in MOF-mediated ERK1/2 phosphorylation.

Prdx1 KO Raw264.7 cells exhibited elevated ERK1/2 and p38, but not AKT, phosphorylation upon LPS stimulation (Figure S4D). Complementation of *Prdx1* KO cells with PRDX1 mutants (Figure 4M) showed that the K197R mutant, but not WT or K197Q mutant, augmented ERK1/2 phosphorylation following 30 min of LPS stimulation (Figure 4N). Remarkably, the K197Q, but not WT or K197R, mutant diminished ERK1/2 phosphorylation following 1 h of LPS stimulation (Figure 4N), suggesting that constitutively acetylated PRDX1 leads to a shorter induction of ERK1/2 phosphorylation compared to WT PRDX1. This aligns with our previous finding that the K197Q mutant has better hydrogen peroxide-scavenging ability than WT upon prolonged hydrogen peroxide exposure or 3 h of LPS stimulation (Figures 3B, 3H, and 3K). p38, AKT, or c-Jun N-terminal kinase (JNK) phosphorylation in the PRDX1 complementation assay were affected by the PRDX1 K197 acetylation status (Figure 4N), suggesting that PRDX1 K197ac may be responsible for rendering the specificity of hydrogen peroxide signaling toward the regulation of kinase activity. It is possible that this could result from compartmentalized regulation of hydrogen peroxide levels by PRDX1 K197ac (Figure 3K). Furthermore, HDAC6 inhibition by tubacin (Figures 1H, 3I, and S4E) specifically reduced ERK1/2 phosphorylation in response to LPS (Figure S4E), accentuating the reversibility of the effect of PRDX1 K197ac on ERK1/2 activation. Taken together, we showed that the absence of PRDX1 K197ac augments LPS-induced ERK1/2 phosphorylation, whereas the presence of PRDX1 K197ac attenuates ERK1/2 phosphorylation. We hypothesize that, in nature, LPS-induced reduction of PRDX1 K197ac (Figures 2B–2E) enables cells to sense and transmit signals from the cell surface via increase of local hydrogen peroxide concentration and subsequent ERK1/2 phosphorylation.

LPS-induced decrease of PRDX1 K197 acetylation boosts glycolysis

Inflammatory macrophages undergo metabolic reprogramming toward glycolysis to sustain their function. Given that the ERK1/2 signaling cascade has been implicated in stimulating glycolysis in cancer cells,[61] we examined the impact of MOF-mediated PRDX1 K197ac on glycolytic metabolism in LPS-induced macrophages. Using Seahorse glycolysis stress assay, we measured extracellular acidification rate (ECAR) as a proxy for lactate production and found that MOF-depleted BMDMs stimulated with LPS for 3 h showed enhanced glycolytic capacity (Figures 5A, 5B, and S5A). Pre-treatment with U0126, a selective MEK1/2 inhibitor that specifically abolishes ERK1/2 phosphorylation (Figure S5B), diminished the increased glycolytic capacity from LPS-stimulated as well as LPS-stimulated and MOF-depleted macrophages (Figures 5A and 5B), suggesting that MOF contributes to LPS-stimulated glycolytic metabolism. U0126 inhibition did not abolish LPS-induced glycolysis, confirming the involvement of other pathways, such as the AKT pathway,[7,9,11] which is independent of MOF. U0126 inhibition did not lower LPS-stimulated glycolysis in MOF-depleted BMDMs to control levels, suggesting MOF might regulate glycolysis through ERK1/2-independent mechanisms. These findings underscore the intricate regulation of glycolysis in response to LPS.

RNA sequencing of MOF-depleted BMDMs, with or without LPS stimulation, showed unchanged transcript levels of glycolysis enzymes (Figures 5C and 5D), suggesting MOF-induced enhanced glycolysis upon LPS stimulation is post-transcriptional. Moreover, MOF-depleted BMDMs pre-treated with NAC (Figure S4C) exhibited reduced glycolytic capacity upon LPS stimulation (Figure 5E), suggesting a ROS-dependent mechanism. Overexpression of WT MOF decreased glycolytic capacity upon LPS stimulation, while enzymatically inactive MOF (E350Q) increased it, suggesting the enzymatic activity of MOF is involved (Figure S5C).

To investigate the role of PRDX1 and PRDX1 K197 acetylation in glycolysis, BMDMs depleted of PRDX1 or over-expressing

(H) Schematic illustration of LPS-induced pathways analyzed via western blot in the following analyses.
(I and J) MAPK and AKT activation analysis of MOF-depleted BMDMs stimulated with LPS (100 ng/mL) for the indicated times (hours). Band intensities of phosphorylated and total kinase from three independent experiments were quantified and relative ratio of phosphorylated to total protein normalized to control (shCTRL, t = 0 h) were analyzed with two-way ANOVA followed by Sidak's multiple comparison test.
(K) Schematic illustration of MAPK pathways.
(L) MA plot of genes encoding MAPK pathway kinases from RNA-seq in MOF-depleted BMDMs stimulated with LPS or unstimulated. Red dots, DEGs; green dots, MAPK pathway kinases. Log2FC (shMOF/shCTRL) and –log(padj) of green dots in MA plot are shown in the dot plot.
(M) Schematic illustration of complementation assay in *Prdx1* KO Raw264.7 cells.
(N) MAPK and AKT activation analysis of *Prdx1* KO Raw264.7 cells complemented with EV or WT, K197R, or K197Q PRDX1-expressing plasmids in response to LPS (100 ng/mL) at indicated time (hours).

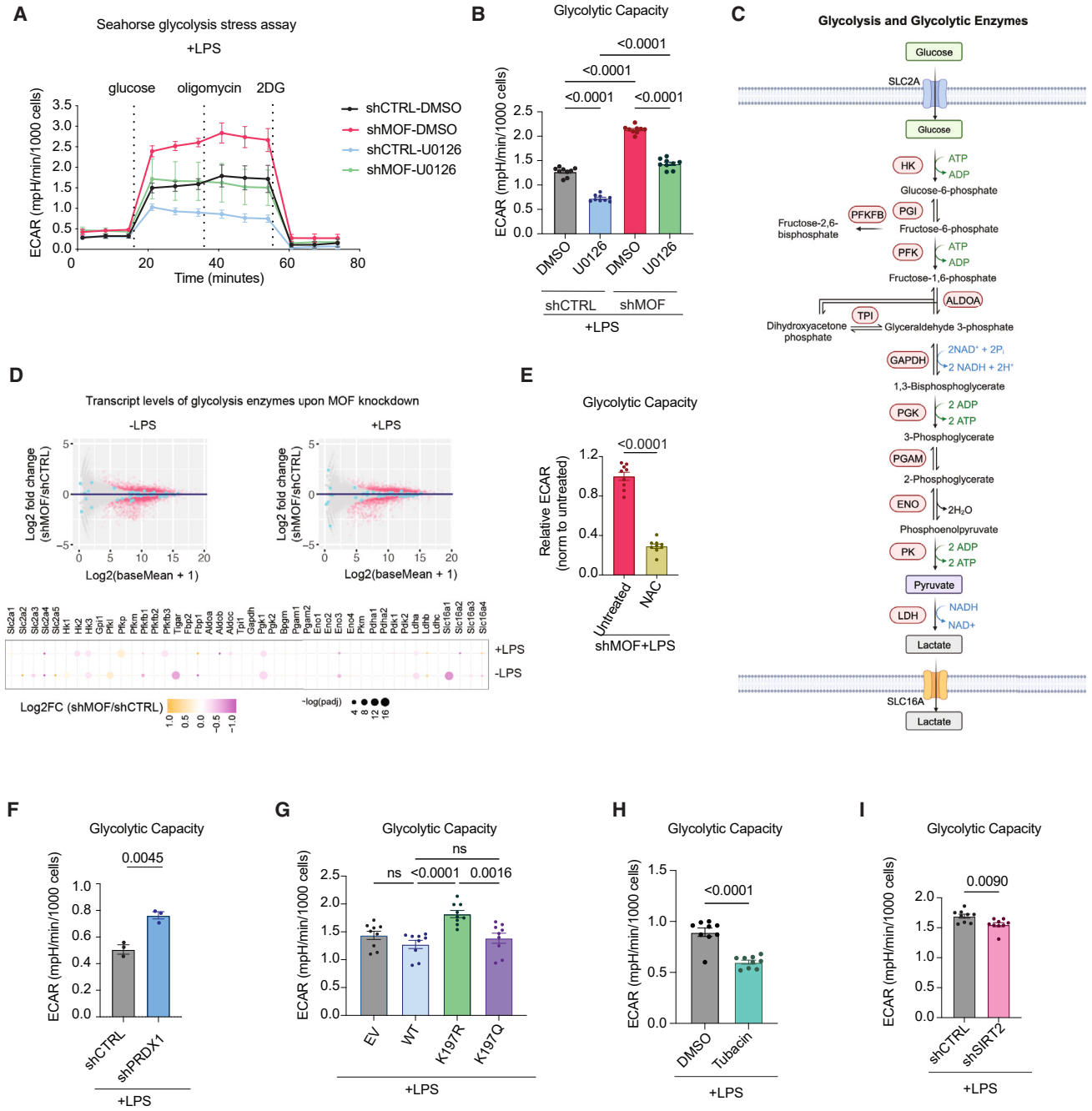

Figure 5. LPS-induced decrease of PRDX1 K197 acetylation boosts glycolysis

(A and B) Seahorse glycolysis stress assay (A) and glycolytic capacity (B) of MOF-depleted BMDMs pre-treated with 10 μM U0126 or DMSO for 18 h followed by LPS stimulation (100 ng/mL, 3 h).

(C) Schematic illustration of enzymes in glycolysis.

(D) MA plot of glycolytic enzyme genes from RNA-seq in MOF-depleted BMDMs stimulated with LPS (100 ng/mL, 3 h) or unstimulated. Red dots, DEGs; green dots, glycolytic enzymes. Log2FC (shMOF/shCTRL) and –log(padj) of green dots in MA plot are shown in the dot plot.

(E–I) Glycolytic capacity of MOF-depleted BMDMs pre-treated with 10 mM NAC or untreated for 18 h followed by LPS stimulation (100 ng/mL, 3 h) (E); PRDX1-depleted BMDMs followed by LPS stimulation (100 ng/mL, 3 h) (F); BMDMs lentivirally transduced with EV, WT, K197R, or K197Q PRDX1 followed by LPS stimulation (100 ng/mL, 3 h) (G); BMDMs pre-treated with 16 μM tubacin or DMSO for 18 h followed by LPS stimulation (100 ng/mL, 3 h) (H); and SIRT2-depleted BMDMs followed by LPS stimulation (100 ng/mL, 3 h) (I).

n = 9, three independent samples in triplicate (B, E, G–I). *n* = 3, three independent samples (F). Data shown as mean ± SEM and analyzed with either one-way ANOVA followed by Tukey's multiple comparisons test (B and G) or two-tailed unpaired t test (E, F, H, and I).

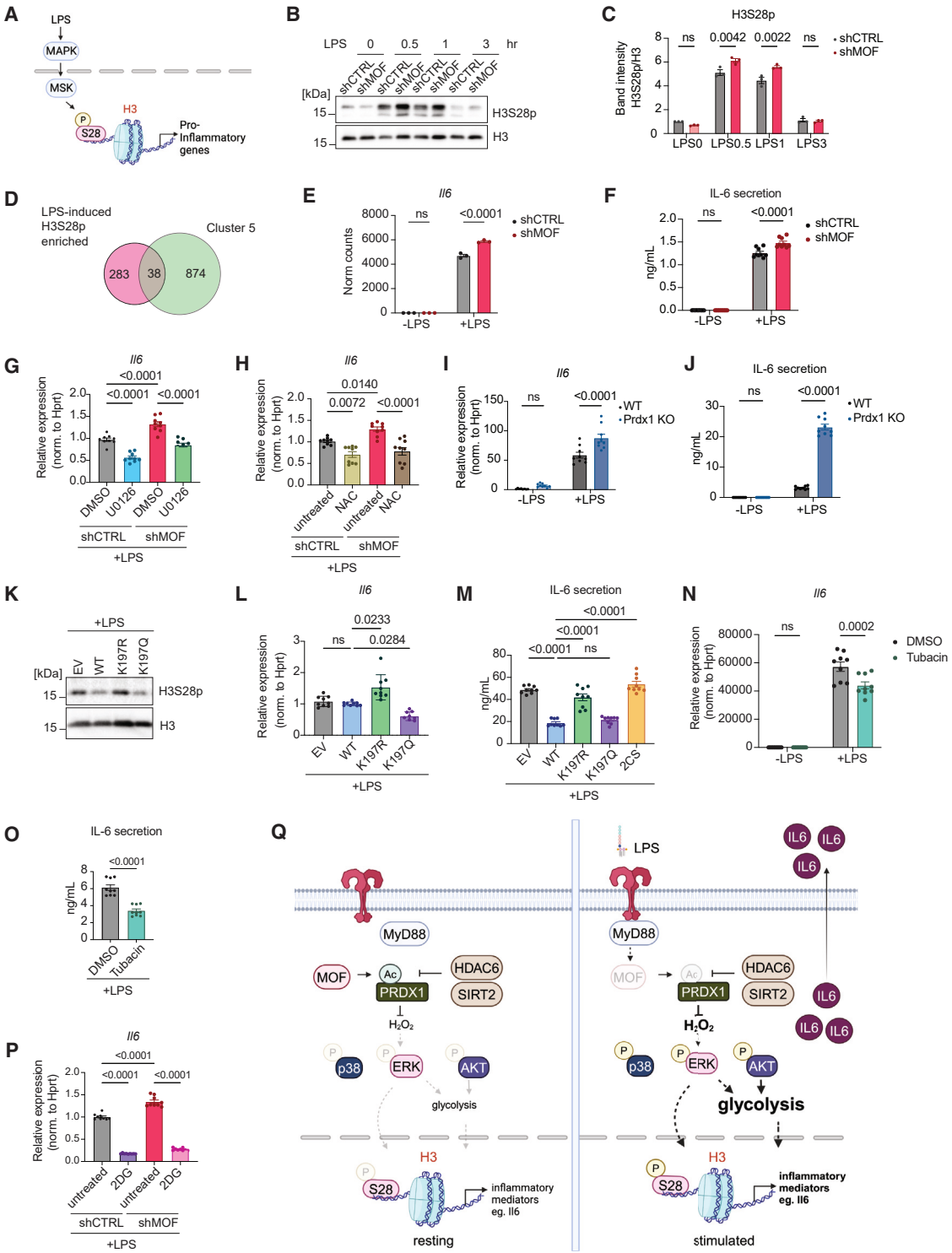

Figure 6. LPS-induced decrease of PRDX1 K197 acetylation potentiates production of the pro-inflammatory cytokine IL-6

(A) Schematic illustrating LPS-induced MAPK signaling to chromatin such as H3S28p, for inducible transcription in macrophage.

(B and C) Western blot for H3S28p of MOF-depleted BMDMs stimulated with LPS (100 ng/mL) at indicated time (hours) (B). Band intensities were quantified and relative levels of H3S28p/H3 normalized to control (C).

(D) Venn diagram showing overlap between LPS-induced H3S28p-enriched genes from dataset GSE63792 and LPS-induced MOF-augmented genes (cluster 5); 38 genes are shared.

(legend continued on next page)

WT, K197R, or K197Q PRDX1 mutants were utilized. Firstly, PRDX1-depleted BMDMs showed enhanced glycolytic capacity upon LPS stimulation (Figure 5F), suggesting the involvement of PRDX1 in regulation of glycolysis during inflammatory macrophage activation. Secondly, overexpression of K197R, but not WT or K197Q PRDX1 in BMDMs elevated glycolytic capacity upon LPS stimulation (Figure 5G), indicating that PRDX1 K197 acetylation status regulates glycolysis. In addition, BMDMs pre-treated with tubacin (Figure 5H) or depleted of SIRT2 (Figure 5I) showed increased glycolytic capacity in response to LPS, highlighting the reversible regulation of glycolytic capacity via PRDX1 K197ac. Taken together, these results suggest that loss of MOF or PRDX1 K197ac enhances glycolytic capacity, while PRDX1 K197ac limits it in response to LPS.

LPS-induced decrease of PRDX1 K197 acetylation potentiates production of the pro-inflammatory cytokine IL-6

The LPS-triggered MAPK signaling cascade can phosphorylate histone proteins such as H3 at serine 28 (H3S28p), leading to rapid transcription of inflammatory genes such as *Il6*[62] (Figure 6A). Given MOF-mediated PRDX1 K197ac modulates LPS-induced ERK1/2 activation, we investigated whether MOF-mediated PRDX1 acetylation regulates inflammatory genes via H3S28p. Firstly, MOF-depleted BMDMs showed augmented H3S28p at 30–60 min after LPS exposure (Figures 6B and 6C), parallel to the timing of induction of ERK1/2 signaling (Figure 4H). Secondly, 38 of the MOF-sensitive, LPS-induced genes (Figure 4F, cluster 5) overlap with LPS-induced H3S28p-enriched genes (Figures 6D and S6A). We further selected *Il6* from cluster 5 to investigate whether PRDX1 K197ac influences its expression. MOF depletion increased not only *Il6* transcript levels (Figure 6E) but also secretion level (Figure 6F). Inhibition of ERK1/2 using U0126 attenuated the induction of *Il6* expression observed following LPS treatment as well as following depletion of MOF in LPS-treated BMDMs (Figure 6G), indicating that the MOF-mediated ERK1/2 signaling cascade contributes to this transcriptional upregulation. Moreover, scavenging cellular ROS by NAC also diminished the induction of *Il6* expression by LPS and by depletion of MOF in LPS-treated BMDMs (Figure 6H), suggesting that ROS contributes to this process.

Prdx1 KO in Raw264.7 macrophages augmented LPS-induced *Il6* expression (Figure 6I) and secretion of IL-6 (Figure 6J), phenocopying the effects of MOF depletion in BMDMs (Figures 6E and 6F). The complementation assay demonstrated that K197R, but not K197Q, PRDX1 mutant increased bulk levels of H3S28p (Figure 6K), *Il6* expression (Figure 6L), and secretion of IL-6 (Figure 6M) in response to LPS, suggesting that PRDX1 K197ac regulates LPS-induced *Il6* production via H3S28p. Given H4K16ac is the major substrate of MOF and functions in transcriptional activation, we examined whether PRDX1 K197ac affects H4K16ac. *Prdx1* KO cells complemented with PRDX1 K197R or K197Q mutants exhibited no change in bulk H4K16ac level in response to LPS (Figure S6B), suggesting that the transcriptional regulation of *Il6* elicited by PRDX1 K197ac is unlikely to be mediated through modulation of H4K16ac bulk levels. HDAC6 inhibition by tubacin diminished LPS-induced *Il6* expression (Figure 6N) and IL-6 secretion (Figure 6O), indicating the reversibility of PRDX1 K197ac-modulated IL-6 production. Furthermore, inhibition of glycolysis by 2-deoxy-d-glucose (2-DG), a glycolysis inhibitor, abrogated LPS-induced and/or MOF-mediated *Il6* expression (Figure 6P), suggesting that MOF-sensitive glycolysis contributes to LPS-induced *Il6* expression. Together, these results suggest that loss of MOF or PRDX1 K197ac enhances the bulk level of H3S28p and thus IL-6 production, while PRDX1 K197ac limits it in response to LPS.

DISCUSSION

Here, we describe the MOF/PRDX1/ERK axis, which regulates macrophage activation at both metabolic and transcriptional levels. By identifying PRDX1 as a new substrate for MOF, we demonstrate that MOF tunes LPS-induced macrophage activation via PRDX1 acetylation at lysine 197. Mechanistically, in immediate response to LPS, MOF protein is reduced and thus PRDX1 K197ac is decreased. LPS-induced decrease of PRDX1 K197ac impairs its peroxidase activity, increasing

(E) Normalized counts of *Il6* from RNA-seq.
(F) IL-6 ELISA assay for culture supernatants from MOF-depleted BMDMs stimulated with LPS (100 ng/mL, 3 h) or unstimulated.
(G and H) RT-qPCR for *Il6* mRNA in MOF-depleted BMDMs pre-treated with 10 μM U0126 for 18 h (G) or pre-treated with 10 mM NAC for 18 h (H) followed by LPS stimulation (100 ng/mL, 3 h).
(I) RT-qPCR for *Il6* mRNA in *Prdx1* KO Raw264.7 cells stimulated with LPS (100 ng/mL, 3 h) or unstimulated.
(J) IL-6 ELISA assay for culture supernatants from *Prdx1* KO Raw264.7 cells stimulated with LPS (100 ng/mL, 3 h) or unstimulated.
(K) Western blot for H3S28p in *Prdx1* KO Raw264.7 cells complemented with EV or WT, K197R, or K197Q PRDX1 stimulated with LPS (100 ng/mL, 1 h).
(L) RT-qPCR for *Il6* mRNA in *Prdx1* KO Raw264.7 cells complemented with EV or WT, K197R, or K197Q PRDX1 stimulated with LPS.
(M) IL-6 ELISA assay for culture supernatants from *Prdx1* KO Raw264.7 cells complemented with EV or WT, K197R, or K197Q PRDX1 stimulated with LPS (100 ng/mL, 3 h).
(N) RT-qPCR for *Il6* mRNA in BMDMs pre-treated with 16 μM tubacin or DMSO for 18 h followed by LPS stimulation (100 ng/mL, 3 h) or unstimulated.
(O) IL-6 ELISA assay for culture supernatants from BMDMs pre-treated with 16 μM tubacin or DMSO for 18 h followed by LPS stimulation (100 ng/mL, 3 h).
(P) RT-qPCR for *Il6* mRNA in MOF-depleted BMDMs pre-treated with 5 mM hexokinase inhibitor 2-deoxy-d-glucose (2-DG) for 1 h followed by LPS stimulation (100 ng/mL, 3 h).
(Q) MOF-mediated K197 acetylation of PRDX1 regulates inflammatory macrophage activation. Reduced MOF protein upon LPS stimulation decreases PRDX1 K197 acetylation, leading to elevated hydrogen peroxide and activation of ERK1/2 signaling. This cascade enhances glycolysis and H3S28p, potentiating IL-6 production in activated macrophages.
$n = 9$, three independent samples in triplicate (F–J and L–P). Data shown as mean ± SEM analyzed with two-way ANOVA followed by Sidak's multiple comparison test (C, E, F, I, J, and N), one-way ANOVA followed by Dunn's multiple comparisons test (G, H, L, M, and P) or two-tailed unpaired t test (O).

cellular hydrogen peroxide accumulation, which enhances ERK1/2 phosphorylation. This signaling cascade boosts glycolytic metabolism of macrophages and primes transcription for inflammatory cytokine production. Notably, PRDX1 K197 acetylation responds to LPS, but not to IL-4 or IL-10, suggesting that MOF/PRDX1/ERK axis specifically pertains to inflammatory macrophages. Interestingly, while IL-4 can induce ERK1/2 phosphorylation through a STAT6-independent pathway,[63–65] neither MOF protein levels nor PRDX1 K197ac are affected by IL-4 stimulation. This underscores that MOF-dependent PRDX1 K197ac constitutes a specific upstream mechanism for the ERK1/2 signaling cascade in inflammatory macrophages.

PTMs are crucial for protein structure, stability, localization, interactions, and functions, closely tied to molecular regulation in various cellular processes.[66,67] We show that acetylation of PRDX1 enhances its resistance to inactivation of peroxidase activity caused by hyperoxidation. Initially, K197 acetylation does not significantly affect the monomer-to-dimer ratio but lowers the hyperoxidation level. Upon prolonged hydrogen peroxide challenge, K197 acetylation increases resistance to hyperoxidation and results in a higher proportion of monomeric, likely reduced, PRDX1. Our findings align with previous studies showing the acetylation of peroxiredoxins (PRDX1 or PRDX2) leads to increased peroxidase activity,[29,30] and enhanced resistance to hyperoxidation upon persistent hydrogen peroxide exposure.[30] Collectively, PRDX1 K197ac enhances resistance to hyperoxidation and thus may increase the proportion of PRDX1 found in the reduced form, leading to the observed elevation in peroxidase activity of PRDX1.

The PRDX1 catalytic cycle begins with hydrogen peroxide binding in the fully folded (FF) active site. The peroxide oxidizes the peroxidatic cysteine to sulfenic acid. A resolving thiol on another PRDX1 molecule then reacts with the sulfenic acid, releasing water and forming a disulfide bond. This requires the sulfenic acid to transition to a locally unfolded (LU) conformation, preventing reversion to the FF state. Trx or other small-molecule thiols reduce the disulfide, regenerating free thiols, allowing the FF active site to refold and prepare PRDX1 for subsequent catalytic cycles.[68] We speculate that K197ac may affect local protein conformation of PRDX1 or interaction with Trx during catalysis and thus prevent hyperoxidation. In addition, our *in vitro* HAT assay shows a decrease of PRDX1 K197ac in the 2CS mutant, implying that cysteine 53 and cysteine 173 boost its acetylation at lysine 197. This implies a crosstalk between cysteine 52 and/or 173 and lysine 197. Of note, the latest structural report on the oxidized and reduced state of a transaldolase enzyme of *Neisseria gonorrhoeae* discovers a covalent crosslink between a cysteine and a lysine residue. This covalent crosslink serves as a structurally allosteric switch for its enzymatic activity.[69] In light of this observation, we speculate that acetylation at lysine 197 may similarly act as an allosteric switch in response to redox alterations.

While acetylation stands as the second most frequent PTM in proteins,[70] its role in signaling transduction (excluding transcription factor and histone protein) is less explored compared to phosphorylation.[71–76] We demonstrate that PRDX1 K197ac regulates ERK1/2 phosphorylation during TLR4 signaling. PRDX1 is known to modulate hydrogen peroxide levels, affecting cysteine oxidation of target proteins such as kinases or phosphatases, and thus mediating signal transduction, particularly in the context of exogenous addition of hydrogen peroxide or growth factors in cancer cells.[8,14–25] However, the regulation of hydrogen peroxide signaling in macrophage under physiological cellular hydrogen peroxide induction conditions remains largely uncharacterized. Moreover, the action of PRDX1 depends on stimuli type, exposure period, local hydrogen peroxide concentration, subcellular localization of targets, and cellular context.[25,77] It is not known how molecular mechanisms underpinning PRDX1 achieve the specificity for signal transduction. Our study shows K197 acetylation selectively affects the plasma membrane pool of hydrogen peroxide without significantly impacting cytoplasmic or nuclear pools, indicating a compartmentalized regulation. Unlike *Prdx1* knockout, which induces global MAPK activation in macrophages, LPS-induced reduction of PRDX1 K197ac selectively enhances ERK1/2 activation without affecting p38 or AKT activation in TLR4 signaling, corroborating that specificity in kinase activation by PRDX1 K197ac might associate with compartmentalized regulation of hydrogen peroxide concentration. Indeed, our subcellular fractionation results reveal diminished cytoplasmic and membrane fraction of PRDX1 K197ac upon LPS challenge rather than nuclear fraction. Earlier research indicates subcellular localization determines MAPK signaling output.[28,78] We propose that PRDX1 near the plasma membrane represents the main subpopulation of the protein, which changes its K197 acetylation status in response to LPS and drives specificity in ERK1/2 modulation in macrophages. This aligns with studies showing PRDX1 phosphorylation at specific subcellular locations for growth factor signal transduction and mitotic progression.[32,79]

Extensive studies demonstrate metabolic reprograming to glycolysis drives LPS-induced macrophage activation, particularly in longer-term exposure scenarios.[80–85] However, initial signaling mechanisms orchestrating this shift remain poorly understood. In early LPS response, Myd88 and TRIF play crucial roles in triggering glycolysis in macrophages.[10] Upon TLR stimulation, the TBK/IKKε-AKT pathway rapidly stimulates glycolytic metabolism to support dendritic cell activation and function.[9,11] Here, we introduce a Myd88 and TRIF downstream signaling cascade involving the MOF/PRDX1/ERK axis that facilitates early glycolytic engagement in LPS-activated macrophages. While ERK1/2 activation has been implicated in stimulating glycolysis in cancer cells,[61,86,87] the crosstalk between ERK activation and glycolysis in macrophages requires further exploration. Our findings illustrate MOF-mediated PRDX1 K197ac contributes to LPS-induced glycolysis. Moreover, our results show AKT activation is unaffected by MOF-mediated PRDX1 K197ac, suggesting that the AKT pathway alone does not fully account for promoting glycolytic metabolism in early LPS response. Of note, ERK1/2 inhibition via U0126 in MOF-depleted BMDMs could not reduce LPS-stimulated glycolysis to the level observed in the control, indicating that MOF may contribute to glycolysis via other mechanisms. In fact, recent studies show that loss of MOF reduces mitochondrial OXPHOS[88] and fatty acid β-oxidation,[89] hinting that attenuated mitochondrial activity

upon loss of MOF may also contribute to the augmentation of glycolysis.

Recent work indicates rapid induction of histone modifications, such as H3S28p[62] and H3.3S31p,[90] upon LPS stimulation, promoting inflammatory gene expression in macrophages. For instance, H3S28p is mediated by MSK1/2, which are downstream kinases of p38 and ERK1/2, and is enriched at the promoters and enhancers of LPS-induced genes, stimulating transcription.[91] Our study reveals MOF depletion increases H3S28p levels following LPS stimulation. Interestingly, only a subset (11%) of H3S28p-enriched genes are affected by MOF depletion, suggesting involvement of other kinase cascades such as p38, which MOF depletion does not impact. Future work is warranted to investigate whether H3.3S31p is affected by MOF and to identify the MOF-sensitive chromatin regions of H3S28p. Our study highlights IL-6 as an illustrative example of a H3S28p-enriched, MOF-sensitive, and PRDX1 K197 acetylation-sensitive gene. IL-6 plays a pivotal role in immune homeostasis, hematopoiesis, regulating inflammation, supporting development, and modulating metabolism.[92,93] Dysregulated IL-6 production is implicated in the onset of chronic inflammation and autoimmune diseases[92] and linked to persistent phenotypes in COVID-19 infection.[94] Our study suggests that antagonism of MOF-mediated PRDX1 K197ac events, such as HDAC6 or SIRT2 inhibition, can reversibly regulate IL-6 production, providing new therapeutic targets for treating IL-6-associated diseases.

Overall, we identified MOF as a regulator of macrophage activation through PRDX1 acetylation at lysine 197. Our findings also fill a gap in our knowledge about the specificity in MAPK pathway in response to stress and initial signaling cascade to stimulate glycolysis in macrophages. We propose that MOF-mediated PRDX1 K197ac acts as a signaling hub in inflammatory macrophages, modulating glycolytic metabolism and inflammatory gene transcription, at least in part via ERK1/2 (Figure 6Q). The selective responsiveness of PRDX1 K197ac also renders targets aimed at the inflammatory but not anti-inflammatory macrophage subpopulation.

Limitations of the study

We show that PRDX1 K197ac affects ERK1/2 activation via hydrogen peroxide based on the current understanding that ERK1/2 oxidation occurs at low hydrogen peroxide concentrations (0.1 μM).[23,95] Our study lacks direct evidence that PRDX1 K197ac impacts ERK1/2 oxidation. Future work is warranted to identify MOF-mediated PRDX1 K197ac-sensitive ERK1/2 oxidation sites using cysteine redox proteomics. Investigating ERK1/2 substrates sensitive to MOF-mediated PRDX1 K197ac can elucidate the detailed mechanism of PRDX1 K197ac in glycolysis and transcriptional regulation, and thus phosphoproteome experiments are warranted.

RESOURCE AVAILABILITY

Lead contact

Further information and requests for resources and reagents should be directed to and will be fulfilled by the lead contact, Asifa Akhtar (akhtar@ie-freiburg.mpg.de).

Materials availability

The materials will be available from the lead contact with a completed Materials Transfer Agreement.

Data and code availability

- All data needed to evaluate the conclusions in the paper are present in the paper and/or the supplemental information. RNA-seq. data are available in GEO under GSE231941. Proteome data are available in PRIDE under PXD046284.
- This paper does not report original code.
- Any additional information required to reanalyze the data reported in this work paper is available from the lead contact upon request.

ACKNOWLEDGMENTS

We thank past and present members of the Asifa Akhtar laboratory for their discussions and technical support. We appreciate Prof. Sang Won Kang (Ewha Womans University, South Korea) for providing yTrx and yTrxR plasmids and Dr. Tim Lämmermann for supplying L929 mouse fibroblast cells and aiding in BMDM generation. We also acknowledge Dr. Angelika Rambold and Dr. Lämmermann for their feedback on the manuscript. The FACS, imaging, deep sequencing, bioinformatics, and animal facility at MPI-IE were crucial to this project. Illustrations were created with BioRender.com.

Funding: this work was also supported by the Deutsche Forschungsgemeinschaft (DFG, German Research Foundation) under SFB1381 (project ID 403222702), CRC 992 (A02), CRC 1425 (P04), awarded to A.A.

AUTHOR CONTRIBUTIONS

A.A. and H.-R.C. conceived the study. H.-R.C. designed and performed the experiments and analyzed the data. T.R. performed the HPLC experiments. G.M. performed the MS experiments and analyzed the data. Y.S. performed bioinformatic analyses. H.-R.C. wrote the manuscript. M.S. edited and revised the manuscript. R.G. critically discussed results and edited the manuscript. A.A. supervised the project. All authors reviewed, edited, and approved the paper.

DECLARATION OF INTERESTS

The authors declare no competing interests.

STAR★METHODS

Detailed methods are provided in the online version of this paper and include the following:

- KEY RESOURCES TABLE
- EXPERIMENTAL MODEL AND STUDY PARTICIPANT DETAILS
  - Generation and activation of bone marrow-derived macrophages
  - Cell culture
  - Animal experiments
- METHOD DETAILS
  - Generation of anti-PRDX1 K197ac antibody
  - Plasmid construction
  - Production of L929 conditioned medium
  - Generation of lentiviral particles
  - CRISPR-Cas9-mediated gene knockout
  - Subcellular fractionation and Western blot
  - Reverse transcription followed by quantitative PCR
  - RNA sequencing analysis
  - Recombinant protein expression and purification
  - *In vitro* peroxidase assay
  - *In vitro* HAT assay
  - Mass spectrometry
  - Measurement of extracellular acidification rates (ECAR)
  - Peroxy Orange 1 staining
  - Enzyme-linked immunosorbent assay (ELISA)

- HyPer7 measurements
- Immunofluorescence
- Redox state assessment of PRDX1

- QUANTIFICATION AND STATISTICAL ANALYSIS

SUPPLEMENTAL INFORMATION

Supplemental information can be found online at https://doi.org/10.1016/j.celrep.2024.114682.

Received: October 9, 2023
Revised: June 27, 2024
Accepted: August 9, 2024
Published: August 28, 2024

REFERENCES

1. Shapouri-Moghaddam, A., Mohammadian, S., Vazini, H., Taghadosi, M., Esmaeili, S.-A., Mardani, F., Seifi, B., Mohammadi, A., Afshari, J.T., and Sahebkar, A. (2018). Macrophage plasticity, polarization, and function in health and disease. J. Cell. Physiol. *233*, 6425–6440. https://doi.org/10.1002/jcp.26429.
2. Wynn, T.A., and Vannella, K.M. (2016). Macrophages in Tissue Repair, Regeneration, and Fibrosis. Immunity *44*, 450–462. https://doi.org/10.1016/j.immuni.2016.02.015.
3. Lawrence, T., and Natoli, G. (2011). Transcriptional regulation of macrophage polarization: enabling diversity with identity. Nat. Rev. Immunol. *11*, 750–761. https://doi.org/10.1038/nri3088.
4. Galván-Peña, S., and O'Neill, L.A.J. (2014). Metabolic Reprograming in Macrophage Polarization. Front. Immunol. *5*, 420. https://doi.org/10.3389/fimmu.2014.00420.
5. Ginhoux, F., Schultze, J.L., Murray, P.J., Ochando, J., and Biswas, S.K. (2016). New insights into the multidimensional concept of macrophage ontogeny, activation and function. Nat. Immunol. *17*, 34–40. https://doi.org/10.1038/ni.3324.
6. Martinez, F.O., and Gordon, S. (2014). The M1 and M2 paradigm of macrophage activation: time for reassessment. F1000Prime Rep. *6*, 13. https://doi.org/10.12703/p6-13.
7. Langston, P.K., Shibata, M., and Horng, T. (2017). Metabolism Supports Macrophage Activation. Front. Immunol. *8*, 61. https://doi.org/10.3389/fimmu.2017.00061.
8. Pérez, S., and Rius-Pérez, S. (2022). Macrophage Polarization and Reprogramming in Acute Inflammation: A Redox Perspective. Antioxidants *11*, 1394. https://doi.org/10.3390/antiox11071394.
9. Covarrubias, A.J., Aksoylar, H.I., and Horng, T. (2015). Control of macrophage metabolism and activation by mTOR and Akt signaling. Semin. Immunol. *27*, 286–296. https://doi.org/10.1016/j.smim.2015.08.001.
10. Lauterbach, M.A., Hanke, J.E., Serefidou, M., Mangan, M.S.J., Kolbe, C.-C., Hess, T., Rothe, M., Kaiser, R., Hoss, F., Gehlen, J., et al. (2019). Toll-like Receptor Signaling Rewires Macrophage Metabolism and Promotes Histone Acetylation via ATP-Citrate Lyase. Immunity *51*, 997–1011.e7. https://doi.org/10.1016/j.immuni.2019.11.009.
11. Everts, B., Amiel, E., Huang, S.C.-C., Smith, A.M., Chang, C.-H., Lam, W.Y., Redmann, V., Freitas, T.C., Blagih, J., van der Windt, G.J.W., et al. (2014). TLR-driven early glycolytic reprogramming via the kinases TBK1-IKKε supports the anabolic demands of dendritic cell activation. Nat. Immunol. *15*, 323–332. https://doi.org/10.1038/ni.2833.
12. Rhee, S.G., and Kil, I.S. (2017). Multiple Functions and Regulation of Mammalian Peroxiredoxins. Annu. Rev. Biochem. *86*, 749–775. https://doi.org/10.1146/annurev-biochem-060815-014431.
13. Lennicke, C., and Cocheme, H.M. (2021). Redox metabolism: ROS as specific molecular regulators of cell signaling and function. Mol. Cell *81*, 3691–3707. https://doi.org/10.1016/j.molcel.2021.08.018.
14. Zhang, Y., Choksi, S., Chen, K., Pobezinskaya, Y., Linnoila, I., and Liu, Z.-G. (2013). ROS play a critical role in the differentiation of alternatively activated macrophages and the occurrence of tumor-associated macrophages. Cell Res. *23*, 898–914. https://doi.org/10.1038/cr.2013.75.
15. Covarrubias, A., Byles, V., and Horng, T. (2013). ROS sets the stage for macrophage differentiation. Cell Res. *23*, 984–985. https://doi.org/10.1038/cr.2013.88.
16. Griess, B., Mir, S., Datta, K., and Teoh-Fitzgerald, M. (2020). Scavenging reactive oxygen species selectively inhibits M2 macrophage polarization and their pro-tumorigenic function in part, via Stat3 suppression. Free Radic. Biol. Med. *147*, 48–60. https://doi.org/10.1016/j.freeradbiomed.2019.12.018.
17. Xu, Q., Choksi, S., Qu, J., Jang, J., Choe, M., Banfi, B., Engelhardt, J.F., and Liu, Z.G. (2016). NADPH Oxidases Are Essential for Macrophage Differentiation. J. Biol. Chem. *291*, 20030–20041. https://doi.org/10.1074/jbc.m116.731216.
18. He, C., Ryan, A.J., Murthy, S., and Carter, A.B. (2013). Accelerated Development of Pulmonary Fibrosis via Cu,Zn-superoxide Dismutase-induced Alternative Activation of Macrophages. J. Biol. Chem. *288*, 20745–20757. https://doi.org/10.1074/jbc.m112.410720.
19. Brüne, B., Dehne, N., Grossmann, N., Jung, M., Namgaladze, D., Schmid, T., Knethen, A. von, and Weigert, A. (2013). Redox Control of Inflammation in Macrophages. Antioxidants Redox Signal. *19*, 595–637. https://doi.org/10.1089/ars.2012.4785.
20. Tan, H.-Y., Wang, N., Li, S., Hong, M., Wang, X., and Feng, Y. (2016). The Reactive Oxygen Species in Macrophage Polarization: Reflecting Its Dual Role in Progression and Treatment of Human Diseases. Oxid. Med. Cell. Longev. *2016*, 2795090. https://doi.org/10.1155/2016/2795090.
21. Sies, H., and Jones, D.P. (2020). Reactive oxygen species (ROS) as pleiotropic physiological signalling agents. Nat. Rev. Mol. Cell Biol. *21*, 363–383. https://doi.org/10.1038/s41580-020-0230-3.
22. Latimer, H.R., and Veal, E.A. (2016). Peroxiredoxins in Regulation of MAPK Signalling Pathways; Sensors and Barriers to Signal Transduction. Mol. Cells *39*, 40–45. https://doi.org/10.14348/molcells.2016.2327.
23. Rhee, S.G., Woo, H.A., and Kang, D. (2018). The Role of Peroxiredoxins in the Transduction of H2O2 Signals. Antioxidants Redox Signal. *28*, 537–557. https://doi.org/10.1089/ars.2017.7167.
24. Cao, J., Schulte, J., Knight, A., Leslie, N.R., Zagozdzon, A., Bronson, R., Manevich, Y., Beeson, C., and Neumann, C.A. (2009). Prdx1 inhibits tumorigenesis via regulating PTEN/AKT activity. EMBO J. *28*, 1505–1517. https://doi.org/10.1038/emboj.2009.101.
25. Kim, Y., and Jang, H.H. (2019). Role of Cytosolic 2-Cys Prx1 and Prx2 in Redox Signaling. Antioxidants *8*, 169. https://doi.org/10.3390/antiox8060169.
26. Kwon, J., Lee, S.-R., Yang, K.-S., Ahn, Y., Kim, Y.J., Stadtman, E.R., and Rhee, S.G. (2004). Reversible oxidation and inactivation of the tumor suppressor PTEN in cells stimulated with peptide growth factors. Proc. Natl. Acad. Sci. USA *101*, 16419–16424. https://doi.org/10.1073/pnas.0407396101.
27. Lee, S.-R., Yang, K.-S., Kwon, J., Lee, C., Jeong, W., and Rhee, S.G. (2002). Reversible Inactivation of the Tumor Suppressor PTEN by H2O2. J. Biol. Chem. *277*, 20336–20342. https://doi.org/10.1074/jbc.m111899200.
28. Galli, S., Antico Arciuch, V.G., Poderoso, C., Converso, D.P., Zhou, Q., Bal de Kier Joffé, E., Cadenas, E., Boczkowski, J., Carreras, M.C., and Poderoso, J.J. (2008). Tumor Cell Phenotype Is Sustained by Selective MAPK Oxidation in Mitochondria. PLoS One *3*, e2379. https://doi.org/10.1371/journal.pone.0002379.
29. Fiskus, W., Coothankandaswamy, V., Chen, J., Ma, H., Ha, K., Saenz, D.T., Krieger, S.S., Mill, C.P., Sun, B., Huang, P., et al. (2016). SIRT2 Deacetylates and Inhibits the Peroxidase Activity of Peroxiredoxin-1 to Sensitize

Breast Cancer Cells to Oxidant Stress-Inducing Agents. Cancer Res. *76*, 5467–5478. https://doi.org/10.1158/0008-5472.can-16-0126.

30. Parmigian, R.B., Xu, W.S., Venta-Perez, G., Erdjument-Bromage, H., Yaneva, M., Tempst, P., and Marks, P.A. (2008). HDAC6 is a specific deacetylase of peroxiredoxins and is involved in redox regulation. Proc. Natl. Acad. Sci. USA *105*, 9633–9638.
31. Chae, H.Z., Oubrahim, H., Park, J.W., Rhee, S.G., and Chock, P.B. (2012). Protein Glutathionylation in the Regulation of Peroxiredoxins: A Family of Thiol-Specific Peroxidases That Function As Antioxidants, Molecular Chaperones, and Signal Modulators. Antioxidants Redox Signal. *16*, 506–523. https://doi.org/10.1089/ars.2011.4260.
32. Woo, H.A., Yim, S.H., Shin, D.H., Kang, D., Yu, D.-Y., and Rhee, S.G. (2010). Inactivation of Peroxiredoxin I by Phosphorylation Allows Localized H2O2 Accumulation for Cell Signaling. Cell *140*, 517–528. https://doi.org/10.1016/j.cell.2010.01.009.
33. Akhtar, A., and Becker, P.B. (2000). Activation of Transcription through Histone H4 Acetylation by MOF, an Acetyltransferase Essential for Dosage Compensation in Drosophila. Mol. Cell *5*, 367–375. https://doi.org/10.1016/s1097-2765(00)80431-1.
34. Smith, E.R., Cayrou, C., Huang, R., Lane, W.S., Côté, J., and Lucchesi, J.C. (2005). A Human Protein Complex Homologous to the Drosophila MSL Complex Is Responsible for the Majority of Histone H4 Acetylation at Lysine 16. Mol. Cell Biol. *25*, 9175–9188. https://doi.org/10.1128/mcb.25.21.9175-9188.2005.
35. Taipale, M., Rea, S., Richter, K., Vilar, A., Lichter, P., Imhof, A., and Akhtar, A. (2005). hMOF Histone Acetyltransferase Is Required for Histone H4 Lysine 16 Acetylation in Mammalian Cells. Mol. Cell Biol. *25*, 6798–6810. https://doi.org/10.1128/mcb.25.15.6798-6810.2005.
36. Singh, M., Bacolla, A., Chaudhary, S., Hunt, C.R., Pandita, S., Chauhan, R., Gupta, A., Tainer, J.A., and Pandita, T.K. (2020). Histone Acetyltransferase MOF Orchestrates Outcomes at the Crossroad of Oncogenesis, DNA Damage Response, Proliferation, and Stem Cell Development. Mol. Cell Biol. *40*, e00232-20. https://doi.org/10.1128/mcb.00232-20.
37. Sheikh, B.N., Guhathakurta, S., and Akhtar, A. (2019). The non-specific lethal (NSL) complex at the crossroads of transcriptional control and cellular homeostasis. EMBO Rep. *20*, e47630. https://doi.org/10.15252/embr.201847630.
38. Sykes, S.M., Mellert, H.S., Holbert, M.A., Li, K., Marmorstein, R., Lane, W.S., and McMahon, S.B. (2006). Acetylation of the p53 DNA-Binding Domain Regulates Apoptosis Induction. Mol. Cell *24*, 841–851. https://doi.org/10.1016/j.molcel.2006.11.026.
39. Kawai, Y., Garduño, L., Theodore, M., Yang, J., and Arinze, I.J. (2011). Acetylation-Deacetylation of the Transcription Factor Nrf2 (Nuclear Factor Erythroid 2-related Factor 2) Regulates Its Transcriptional Activity and Nucleocytoplasmic Localization. J. Biol. Chem. *286*, 7629–7640. https://doi.org/10.1074/jbc.m110.208173.
40. Huai, W., Liu, X., Wang, C., Zhang, Y., Chen, X., Chen, X., Xu, S., Thomas, T., Li, N., and Cao, X. (2019). KAT8 selectively inhibits antiviral immunity by acetylating IRF3. J. Exp. Med. *216*, 772–785. https://doi.org/10.1084/jem.20181773.
41. Luo, H., Shenoy, A.K., Li, X., Jin, Y., Jin, L., Cai, Q., Tang, M., Liu, Y., Chen, H., Reisman, D., et al. (2016). MOF Acetylates the Histone Demethylase LSD1 to Suppress Epithelial-to-Mesenchymal Transition. Cell Rep. *15*, 2665–2678. https://doi.org/10.1016/j.celrep.2016.05.050.
42. Buscaino, A., Köcher, T., Kind, J.H., Holz, H., Taipale, M., Wagner, K., Wilm, M., and Akhtar, A. (2003). MOF-Regulated Acetylation of MSL-3 in the Drosophila Dosage Compensation Complex. Mol. Cell *11*, 1265–1277.
43. Zhou, Y., Schmitz, K.-M., Mayer, C., Yuan, X., Akhtar, A., and Grummt, I. (2009). Reversible acetylation of the chromatin remodelling complex NoRC is required for non-coding RNA-dependent silencing. Nat. Cell Biol. *11*, 1010–1016. https://doi.org/10.1038/ncb1914.
44. Karoutas, A., Szymanski, W., Rausch, T., Guhathakurta, S., Rog-Zielinska, E.A., Peyronnet, R., Seyfferth, J., Chen, H.-R., de Leeuw, R., Herquel, B., et al. (2019). The NSL complex maintains nuclear architecture stability via lamin A/C acetylation. Nat. Cell Biol. *21*, 1248–1260. https://doi.org/10.1038/s41556-019-0397-z.
45. Liu, Y., Zhang, Y.-Y., Wang, S.-Q., Li, M., Long, Y.-H., Li, Y.-F., Liu, Y.-K., Li, Y.-H., Wang, Y.-Q., Mi, J.-S., et al. (2020). WSTF acetylation by MOF promotes WSTF activities and oncogenic functions. Oncogene *39*, 5056–5067. https://doi.org/10.1038/s41388-020-1350-0.
46. Sheikh, B.N., Bechtel-Walz, W., Lucci, J., Karpiuk, O., Hild, I., Hartleben, B., Vornweg, J., Helmstädter, M., Sahyoun, A.H., Bhardwaj, V., et al. (2016). MOF maintains transcriptional programs regulating cellular stress response. Oncogene *35*, 2698–2710. https://doi.org/10.1038/onc.2015.335.
47. Pessoa Rodrigues, C., Chatterjee, A., Wiese, M., Stehle, T., Szymanski, W., Shvedunova, M., and Akhtar, A. (2021). Histone H4 lysine 16 acetylation controls central carbon metabolism and diet-induced obesity in mice. Nat. Commun. *12*, 6212. https://doi.org/10.1038/s41467-021-26277-w.
48. Aeby, E., Ahmed, W., Redon, S., Simanis, V., and Lingner, J. (2016). Peroxiredoxin 1 Protects Telomeres from Oxidative Damage and Preserves Telomeric DNA for Extension by Telomerase. Cell Rep. *17*, 3107–3114. https://doi.org/10.1016/j.celrep.2016.11.071.
49. Ahmed, W., and Lingner, J. (2020). PRDX1 Counteracts Catastrophic Telomeric Cleavage Events That Are Triggered by DNA Repair Activities Post Oxidative Damage. Cell Rep. *33*, 108347. https://doi.org/10.1016/j.celrep.2020.108347.
50. Somyajit, K., Gupta, R., Sedlackova, H., Neelsen, K.J., Ochs, F., Rask, M.-B., Choudhary, C., and Lukas, J. (2017). Redox-sensitive alteration of replisome architecture safeguards genome integrity. Science *358*, 797–802. https://doi.org/10.1126/science.aao3172.
51. Lennicke, C., and Cochemé, H.M. (2021). Redox regulation of the insulin signalling pathway. Redox Biol. *42*, 101964. https://doi.org/10.1016/j.redox.2021.101964.
52. Kim, J.-A., Park, S., Kim, K., Rhee, S.G., and Kang, S.W. (2005). Activity assay of mammalian 2-cys peroxiredoxins using yeast thioredoxin reductase system. Anal. Biochem. *338*, 216–223. https://doi.org/10.1016/j.ab.2004.12.008.
53. Bolduc, J., Koruza, K., Luo, T., Malo Pueyo, J., Vo, T.N., Ezeriņa, D., and Messens, J. (2021). Peroxiredoxins wear many hats: Factors that fashion their peroxide sensing personalities. Redox Biol. *42*, 101959. https://doi.org/10.1016/j.redox.2021.101959.
54. Pak, V.V., Ezeriņa, D., Lyublinskaya, O.G., Pedre, B., Tyurin-Kuzmin, P.A., Mishina, N.M., Thauvin, M., Young, D., Wahni, K., Martínez Gache, S.A., et al. (2020). Ultrasensitive Genetically Encoded Indicator for Hydrogen Peroxide Identifies Roles for the Oxidant in Cell Migration and Mitochondrial Function. Cell Metabol. *31*, 642–653.e6. https://doi.org/10.1016/j.cmet.2020.02.003.
55. Hoehne, M.N., Jacobs, L.J.H.C., Lapacz, K.J., Calabrese, G., Murschall, L.M., Marker, T., Kaul, H., Trifunovic, A., Morgan, B., Fricker, M., et al. (2022). Spatial and temporal control of mitochondrial H2O2 release in intact human cells. EMBO J. *41*, e109169. https://doi.org/10.15252/embj.2021109169.
56. Jezierska-Drutel, A., Attaran, S., Hopkins, B.L., Skoko, J.J., Rosenzweig, S.A., and Neumann, C.A. (2019). The peroxidase PRDX1 inhibits the activated phenotype in mammary fibroblasts through regulating c-Jun N-terminal kinases. BMC Cancer *19*, 812. https://doi.org/10.1186/s12885-019-6031-4.
57. Min, Y., Kim, M.-J., Lee, S., Chun, E., and Lee, K.-Y. (2018). Inhibition of TRAF6 ubiquitin-ligase activity by PRDX1 leads to inhibition of NFKB activation and autophagy activation. Autophagy *14*, 1347–1358. https://doi.org/10.1080/15548627.2018.1474995.
58. Matsumura, K., Iwai, H., Kato-Miyazawa, M., Kirikae, F., Zhao, J., Yanagawa, T., Ishii, T., Miyoshi-Akiyama, T., Funatogawa, K., and Kirikae, T.

(2016). Peroxiredoxin 1 Contributes to Host Defenses against Mycobacterium tuberculosis. J. Immunol. *197*, 3233–3244. https://doi.org/10.4049/jimmunol.1601010.

59. Jarvis, R.M., Hughes, S.M., and Ledgerwood, E.C. (2012). Peroxiredoxin 1 functions as a signal peroxidase to receive, transduce, and transmit peroxide signals in mammalian cells. Free Radic. Biol. Med. *53*, 1522–1530. https://doi.org/10.1016/j.freeradbiomed.2012.08.001.
60. Stöcker, S., Maurer, M., Ruppert, T., and Dick, T.P. (2018). A role for 2-Cys peroxiredoxins in facilitating cytosolic protein thiol oxidation. Nat. Chem. Biol. *14*, 148–155. https://doi.org/10.1038/nchembio.2536.
61. Papa, S., Choy, P.M., and Bubici, C. (2019). The ERK and JNK pathways in the regulation of metabolic reprogramming. Oncogene *38*, 2223–2240. https://doi.org/10.1038/s41388-018-0582-8.
62. Josefowicz, S.Z., Shimada, M., Armache, A., Li, C.H., Miller, R.M., Lin, S., Yang, A., Dill, B.D., Molina, H., Park, H.-S., et al. (2016). Chromatin Kinases Act on Transcription Factors and Histone Tails in Regulation of Inducible Transcription. Mol. Cell *64*, 347–361. https://doi.org/10.1016/j.molcel.2016.09.026.
63. Nelms, K., Keegan, A.D., Zamorano, J., Ryan, J.J., and Paul, W.E. (1999). THE IL-4 RECEPTOR: Signaling Mechanisms and Biologic Functions. Annu. Rev. Immunol. *17*, 701–738. https://doi.org/10.1146/annurev.immunol.17.1.701.
64. Wills-Karp, M., and Finkelman, F.D. (2008). Untangling the Complex Web of IL-4– and IL-13–Mediated Signaling Pathways. Sci. Signal. *1*, pe55. https://doi.org/10.1126/scisignal.1.51.pe55.
65. McCormick, S.M., and Heller, N.M. (2015). Commentary: IL-4 and IL-13 receptors and signaling. Cytokine *75*, 38–50. https://doi.org/10.1016/j.cyto.2015.05.023.
66. Narita, T., Weinert, B.T., and Choudhary, C. (2019). Functions and mechanisms of non-histone protein acetylation. Nat. Rev. Mol. Cell Biol. *20*, 156–174. https://doi.org/10.1038/s41580-018-0081-3.
67. Shvedunova, M., and Akhtar, A. (2022). Modulation of cellular processes by histone and non-histone protein acetylation. Nat. Rev. Mol. Cell Biol. *23*, 329–349. https://doi.org/10.1038/s41580-021-00441-y.
68. Hall, A., Nelson, K., Poole, L.B., and Karplus, P.A. (2011). Structure-based Insights into the Catalytic Power and Conformational Dexterity of Peroxiredoxins. Antioxidants Redox Signal. *15*, 795–815. https://doi.org/10.1089/ars.2010.3624.
69. Wensien, M., von Pappenheim, F.R., Funk, L.-M., Kloskowski, P., Curth, U., Diederichsen, U., Uranga, J., Ye, J., Fang, P., Pan, K.-T., et al. (2021). A lysine–cysteine redox switch with an NOS bridge regulates enzyme function. Nature *593*, 460–464. https://doi.org/10.1038/s41586-021-03513-3.
70. Ramazi, S., and Zahiri, J. (2021). Posttranslational modifications in proteins: resources, tools and prediction methods. Database *2021*, baab012. https://doi.org/10.1093/database/baab012.
71. Fischer, A., Mühlhäuser, W.W.D., Warscheid, B., and Radziwill, G. (2017). Membrane localization of acetylated CNK1 mediates a positive feedback on RAF/ERK signaling. Sci. Adv. *3*, e1700475. https://doi.org/10.1126/sciadv.1700475.
72. Li, Y., Xu, W., McBurney, M.W., and Longo, V.D. (2008). SirT1 Inhibition Reduces IGF-I/IRS-2/Ras/ERK1/2 Signaling and Protects Neurons. Cell Metabol. *8*, 38–48. https://doi.org/10.1016/j.cmet.2008.05.004.
73. Okumura, K., Mendoza, M., Bachoo, R.M., DePinho, R.A., Cavenee, W.K., and Furnari, F.B. (2006). PCAF Modulates PTEN Activity. J. Biol. Chem. *281*, 26562–26568. https://doi.org/10.1074/jbc.m605391200.
74. Ikenoue, T., Inoki, K., Zhao, B., and Guan, K.-L. (2008). PTEN Acetylation Modulates Its Interaction with PDZ Domain. Cancer Res. *68*, 6908–6912. https://doi.org/10.1158/0008-5472.can-08-1107.
75. Sundaresan, N.R., Pillai, V.B., Wolfgeher, D., Samant, S., Vasudevan, P., Parekh, V., Raghuraman, H., Cunningham, J.M., Gupta, M., and Gupta, M.P. (2011). The Deacetylase SIRT1 Promotes Membrane Localization and Activation of Akt and PDK1 During Tumorigenesis and Cardiac Hypertrophy. Sci. Signal. *4*, ra46. https://doi.org/10.1126/scisignal.2001465.
76. Glidden, E.J., Gray, L.G., Vemuru, S., Li, D., Harris, T.E., and Mayo, M.W. (2012). Multiple Site Acetylation of Rictor Stimulates Mammalian Target of Rapamycin Complex 2 (mTORC2)-dependent Phosphorylation of Akt Protein. J. Biol. Chem. *287*, 581–588. https://doi.org/10.1074/jbc.m111.304337.
77. Cho, N.H., Cheveralls, K.C., Brunner, A.-D., Kim, K., Michaelis, A.C., Raghavan, P., Kobayashi, H., Savy, L., Li, J.Y., Canaj, H., et al. (2022). OpenCell: Endogenous tagging for the cartography of human cellular organization. Science *375*, eabi6983. https://doi.org/10.1126/science.abi6983.
78. Harding, A., Tian, T., Westbury, E., Frische, E., and Hancock, J.F. (2005). Subcellular Localization Determines MAP Kinase Signal Output. Curr. Biol. *15*, 869–873. https://doi.org/10.1016/j.cub.2005.04.020.
79. Lim, J.M., Lee, K.S., Woo, H.A., Kang, D., and Rhee, S.G. (2015). Control of the pericentrosomal H 2O 2level by peroxiredoxin I is critical for mitotic progression. J. Cell Biol. *210*, 23–33. https://doi.org/10.1083/jcb.201412068.
80. Kornberg, M.D., Bhargava, P., Kim, P.M., Putluri, V., Snowman, A.M., Putluri, N., Calabresi, P.A., and Snyder, S.H. (2018). Dimethyl fumarate targets GAPDH and aerobic glycolysis to modulate immunity. Science *360*, 449–453. https://doi.org/10.1126/science.aan4665.
81. Diskin, C., Ryan, T.A.J., and O'Neill, L.A.J. (2021). Modification of Proteins by Metabolites in Immunity. Immunity *54*, 19–31. https://doi.org/10.1016/j.immuni.2020.09.014.
82. Tannahill, G.M., Curtis, A.M., Adamik, J., Palsson-McDermott, E.M., McGettrick, A.F., Goel, G., Frezza, C., Bernard, N.J., Kelly, B., Foley, N.H., et al. (2013). Succinate is an inflammatory signal that induces IL-1β through HIF-1α. Nature *496*, 238–242. https://doi.org/10.1038/nature11986.
83. Wang, F., Wang, K., Xu, W., Zhao, S., Ye, D., Wang, Y., Xu, Y., Zhou, L., Chu, Y., Zhang, C., et al. (2017). SIRT5 Desuccinylates and Activates Pyruvate Kinase M2 to Block Macrophage IL-1β Production and to Prevent DSS-Induced Colitis in Mice. Cell Rep. *19*, 2331–2344. https://doi.org/10.1016/j.celrep.2017.05.065.
84. Mills, E.L., Ryan, D.G., Prag, H.A., Dikovskaya, D., Menon, D., Zaslona, Z., Jedrychowski, M.P., Costa, A.S.H., Higgins, M., Hams, E., et al. (2018). Itaconate is an anti-inflammatory metabolite that activates Nrf2 via alkylation of KEAP1. Nature *556*, 113–117. https://doi.org/10.1038/nature25986.
85. Galván-Peña, S., Carroll, R.G., Newman, C., Hinchy, E.C., Palsson-McDermott, E., Robinson, E.K., Covarrubias, S., Nadin, A., James, A.M., Haneklaus, M., et al. (2019). Malonylation of GAPDH is an inflammatory signal in macrophages. Nat. Commun. *10*, 338. https://doi.org/10.1038/s41467-018-08187-6.
86. Lucas, R.M., Luo, L., and Stow, J.L. (2022). ERK1/2 in immune signalling. Biochem. Soc. Trans. *50*, 1341–1352. https://doi.org/10.1042/bst20220271.
87. Lavoie, H., Gagnon, J., and Therrien, M. (2020). ERK signalling: a master regulator of cell behaviour, life and fate. Nat. Rev. Mol. Cell Biol. *21*, 607–632. https://doi.org/10.1038/s41580-020-0255-7.
88. Chatterjee, A., Seyfferth, J., Lucci, J., Gilsbach, R., Preissl, S., Böttinger, L., Mårtensson, C.U., Panhale, A., Stehle, T., Kretz, O., et al. (2016). MOF Acetyl Transferase Regulates Transcription and Respiration in Mitochondria. Cell *167*, 722–738.e23. https://doi.org/10.1016/j.cell.2016.09.052.
89. Khoa, L.T.P., Tsan, Y.-C., Mao, F., Kremer, D.M., Sajjakulnukit, P., Zhang, L., Zhou, B., Tong, X., Bhanu, N.V., Choudhary, C., et al. (2020). Histone Acetyltransferase MOF Blocks Acquisition of Quiescence in Ground-State ESCs through Activating Fatty Acid Oxidation. Cell Stem Cell *27*, 441–458.e10. https://doi.org/10.1016/j.stem.2020.06.005.
90. Armache, A., Yang, S., Martínez de Paz, A., Robbins, L.E., Durmaz, C., Cheong, J.Q., Ravishankar, A., Daman, A.W., Ahimovic, D.J., Klevorn, T., et al. (2020). Histone H3.3 phosphorylation amplifies

stimulation-induced transcription. Nature *583*, 852–857. https://doi.org/10.1038/s41586-020-2533-0.

91. Martínez de Paz, A., and Josefowicz, S.Z. (2021). Signaling-to-chromatin pathways in the immune system. Immunol. Rev. *300*, 37–53. https://doi.org/10.1111/imr.12955.
92. Tanaka, T., Narazaki, M., and Kishimoto, T. (2014). IL-6 in Inflammation, Immunity, and Disease. Csh Perspect Biol *6*, a016295. https://doi.org/10.1101/cshperspect.a016295.
93. Hunter, C.A., and Jones, S.A. (2015). IL-6 as a keystone cytokine in health and disease. Nat. Immunol. *16*, 448–457. https://doi.org/10.1038/ni.3153.
94. Cheong, J.-G., Ravishankar, A., Sharma, S., Parkhurst, C.N., Grassmann, S.A., Wingert, C.K., Laurent, P., Ma, S., Paddock, L., Miranda, I.C., et al. (2023). Epigenetic memory of coronavirus infection in innate immune cells and their progenitors. Cell *186*, 3882–3902.e24. https://doi.org/10.1016/j.cell.2023.07.019.
95. Corcoran, A., and Cotter, T.G. (2013). Redox regulation of protein kinases. FEBS J. *280*, 1944–1965. https://doi.org/10.1111/febs.12224.
96. Pegoraro, G., Kubben, N., Wickert, U., Göhler, H., Hoffmann, K., and Misteli, T. (2009). Ageing-related chromatin defects through loss of the NURD complex. Nat. Cell Biol. *11*, 1261–1267. https://doi.org/10.1038/ncb1971.
97. Baltz, A.G., Munschauer, M., Schwanhäusser, B., Vasile, A., Murakawa, Y., Schueler, M., Youngs, N., Penfold-Brown, D., Drew, K., Milek, M., et al. (2012). The mRNA-Bound Proteome and Its Global Occupancy Profile on Protein-Coding Transcripts. Mol. Cell *46*, 674–690. https://doi.org/10.1016/j.molcel.2012.05.021.
98. Ran, F.A., Hsu, P.D., Wright, J., Agarwala, V., Scott, D.A., and Zhang, F. (2013). Genome engineering using the CRISPR-Cas9 system. Nat. Protoc. *8*, 2281–2308. https://doi.org/10.1038/nprot.2013.143.
99. Adachi, O., Kawai, T., Takeda, K., Matsumoto, M., Tsutsui, H., Sakagami, M., Nakanishi, K., and Akira, S. (1998). Targeted Disruption of the MyD88 Gene Results in Loss of IL-1- and IL-18-Mediated Function. Immunity *9*, 143–150. https://doi.org/10.1016/s1074-7613(00)80596-8.
100. Sheikh, B.N., Guhathakurta, S., Tsang, T.H., Schwabenland, M., Renschler, G., Herquel, B., Bhardwaj, V., Holz, H., Stehle, T., Bondareva, O., et al. (2020). Neural metabolic imbalance induced by MOF dysfunction triggers pericyte activation and breakdown of vasculature. Nat. Cell Biol. *22*, 828–841. https://doi.org/10.1038/s41556-020-0526-8.
101. Bhardwaj, V., Heyne, S., Sikora, K., Rabbani, L., Rauer, M., Kilpert, F., Richter, A.S., Ryan, D.P., and Manke, T. (2019). snakePipes: facilitating flexible, scalable and integrative epigenomic analysis. Bioinformatics *35*, 4757–4759. https://doi.org/10.1093/bioinformatics/btz436.
102. Dobin, A., Davis, C.A., Schlesinger, F., Drenkow, J., Zaleski, C., Jha, S., Batut, P., Chaisson, M., and Gingeras, T.R. (2013). STAR: ultrafast universal RNA-seq aligner. Bioinformatics *29*, 15–21. https://doi.org/10.1093/bioinformatics/bts635.
103. Liao, Y., Smyth, G.K., and Shi, W. (2014). featureCounts: an efficient general purpose program for assigning sequence reads to genomic features. Bioinformatics *30*, 923–930. https://doi.org/10.1093/bioinformatics/btt656.
104. Love, M.I., Huber, W., and Anders, S. (2014). Moderated estimation of fold change and dispersion for RNA-seq data with DESeq2. Genome Biol. *15*, 550. https://doi.org/10.1186/s13059-014-0550-8.
105. Yu, G., Wang, L.-G., Han, Y., and He, Q.-Y. (2012). clusterProfiler: an R Package for Comparing Biological Themes Among Gene Clusters. OMICS A J. Integr. Biol. *16*, 284–287. https://doi.org/10.1089/omi.2011.0118.
106. Montavon, T., Shukeir, N., Erikson, G., Engist, B., Onishi-Seebacher, M., Ryan, D., Musa, Y., Mittler, G., Meyer, A.G., Genoud, C., and Jenuwein, T. (2021). Complete loss of H3K9 methylation dissolves mouse heterochromatin organization. Nat. Commun. *12*, 4359. https://doi.org/10.1038/s41467-021-24532-8.
107. Hein, K., Mittler, G., Cizelsky, W., Kühl, M., Ferrante, F., Liefke, R., Berger, I.M., Just, S., Sträng, J.E., Kestler, H.A., et al. (2015). Site-specific methylation of Notch1 controls the amplitude and duration of the Notch1 response. Sci. Signal. *8*, ra30. https://doi.org/10.1126/scisignal.2005892.
108. Musa, Y.R., Boller, S., Puchalska, M., Grosschedl, R., and Mittler, G. (2018). Comprehensive Proteomic Investigation of Ebf1 Heterozygosity in Pro-B Lymphocytes Utilizing Data Independent Acquisition. J. Proteome Res. *17*, 76–85. https://doi.org/10.1021/acs.jproteome.7b00369.
109. Cox, A.G., Winterbourn, C.C., and Hampton, M.B. (2010). Chapter Four Measuring the Redox State of Cellular Peroxiredoxins by Immunoblotting. Methods Enzymol. *474*, 51–66. https://doi.org/10.1016/s0076-6879(10)74004-0.

STAR★METHODS

KEY RESOURCES TABLE

REAGENT or RESOURCE	SOURCE	IDENTIFIER
Antibodies		
Rabbit Anti-KAT8/MYST1/MOF antibody [EPR15803]	Abcam	Cat# ab200660; RRID:AB_2891127
Rabbit Anti-SIRT2 antibody	Active Motif	Cat# 61045, RRID:AB_2793485
Rabbit Anti-Peroxiredoxin 1 antibody	Abcam	Cat# ab41906, RRID:AB_2284360
Mouse Anti-alpha-Tubulin antibody	Sigma-Aldrich	Cat# T5168, RRID:AB_477579
Rabbit Anti-Lamin B1 antibody	Abcam	Cat# ab16048, RRID:AB_443298
Rabbit Anti-VDAC2 antibody	Cell Signaling Technology	Cat# 9412, RRID:AB_10828727
Mouse Anti-H3 antibody	Active Motif	Cat# 39763, RRID:AB_2650522
Rabbit Anti-Acetylated-Lysine Antibody	Cell Signaling Technology	Cat# 9441, RRID:AB_331805
Mouse Anti-FLAG M2 antibody	Sigma-Aldrich	Cat# F1804, RRID:AB_262044
Rabbit Anti- Phosphor-p38 MAPK (Thr180/Tyr182), Clone 12F8	Cell Signaling Technology	Cat# 4631, RRID:AB_331765
Rabbit Anti-p38 MAPK (D13E1) antibody	Cell Signaling Technology	Cat# 8690, RRID:AB_10999090
Rabbit Anti-Phospho-p44/42 MAPK (Erk1/2) (Thr202/Tyr204) (D13.14.4E) antibody	Cell Signaling Technology	Cat# 4370, RRID:AB_2315112
Rabbit Anti-p44/42 MAPK (Erk1/2) Antibody	Cell Signaling Technology	Cat# 9102, RRID:AB_330744
Rabbit Anti-Phospho-Akt (Ser473) Antibody	Cell Signaling Technology	Cat# 9271, RRID:AB_329825
Rabbit Anti-Akt Antibody	Cell Signaling Technology	Cat# 9272, RRID:AB_329827
Rabbit Anit-Phospho-SAPK/JNK (Thr183/Tyr185) (98F2)	Cell Signaling Technology	Cat# 4671, RRID:AB_331338
Rabbit Anit-SAPK/JNK Antibody	Cell Signaling Technology	Cat# 9252, AB_2250373
Rabbit Anti-Histone H3 (phospho S28) antibody [E191]	Abcam	Cat# ab32388, RRID:AB_732931
Mouse Anti-β-Actin Antibody (C4)	Santa Cruz Biotechnology	Cat# sc-47778 HRP, RRID:AB_2714189
Rabbit Anti-peroxiredoxin-SO3 antibody	Abcam	Cat# ab16830 RRID:AB_443491
Sheep Anti-Mouse IgG, Whole Ab ECL Antibody, HRP Conjugated	Cytiva	Cat# NXA931, RRID:AB_772209
Donkey Anti-Rabbit IgG, Whole Ab ECL Antibody, HRP Conjugated	Cytiva	Cat# NA934, RRID:AB_772206
Rat Anti-mouse F4/80, PE Conjugated	BioLegend	Cat# 123110, RRID:AB_893498)
Rat Anti-mouse/human CD11b, APC/Cyanine7 Conjugated	BioLegend	Cat# 101225, RRID:AB_830641
Goat anti-Mouse IgG (H + L) secondary Antibody, Alexa Fluor™ 488 Conjugated	Thermo Fisher	Cat# A-11029, RRID:AB_2534088
Rabbit Anti-PRDX1 K197ac Antibody	This paper	N/A
Bacterial and virus strains		
Rosetta 2 (DE3) *E. coli*.	Lab strain	N/A
DH5a *E. coli*.	Lab strain	N/A
E. coli. BL21(DE3)	Lab strain	N/A
Chemicals, peptides, and recombinant proteins		
LPS from *E. coli* serotype 0111:B4	Sigma-Aldrich	Cat# L2630
N-acetyl-L-cysteine	Sigma-Aldrich	Cat# A9165
Tubacin	Sigma-Aldrich	Cat# SML0065
Recombinant Murine IL-4	Peprotech	Cat# 214-14
Recombinant Murine IL-10	Peprotech	Cat# 210-10

(*Continued on next page*)

Continued

REAGENT or RESOURCE	SOURCE	IDENTIFIER
2-Deoxy-D-glucose	TCI Chemicals	Cat# D0051
U0126	Cell Signaling Technology	Cat# 9903
Lipofectamine 2000	Thermo Fisher	Cat# 11668019
Peroxy Orange 1	Tocris Bioscience	Cat# 4944
Oligomycin	Thermo Fisher	Cat# 75351
Protein A/G Magnetic beads	Thermo Fisher	Cat# 88802
N-ethylmaleimide	Sigma-Aldrich	Cat# E3876
Catalase from bovine liver	Sigma-Aldrich	Cat# C9322
Wheat Germ Agglutinin Conjugates, Alexa Flour 555	Thermo Fisher	Cat# W32464
Alexa Fluor 647 Phalloidin	Cell Signaling Technology	Cat# 8940S
VECTASHIELD Antifade Mounting Medium with DAPI	Vector Laboratories	Cat# H-1200
Critical commercial assays		
Subcellular protein fractionation kit for cultured cells	Thermo Fisher	Cat# 78840
Illumina TruSeq Stranded mRNA Prep, Ligation	Illumina	Cat# 20040534
Mouse IL-6 ELISA assays	BioLegend	Cat# 431307
Deposited data		
RNA-seq data	This paper	GEO: GSE231941
Proteome data	This paper	PRIDE: PXD046284
Experimental models: Cell lines		
Mouse: primary BMDMs	This paper	N/A
Mouse: Raw264.7 cell line	BIOSS excellence cluster	N/A
Human: HEK293 cell line	BIOSS excellence cluster	N/A
Mouse: L929 cell line	Laboratory of Dr. Tim Lämmermann	N/A
Mouse: Raw264.7 *Prdx1* KO cells	This paper	N/A
Human: HEK293 *Prdx1* KO cells	This paper	N/A
Experimental models: Organisms/strains		
C57BL/6J	The Jackson Laboratory	N/A
Oligonucleotides		
shRNA for human MOF: 5′-CGAAAT TGATGCCTGGTATTTCTCGAGAAAT ACCAGGCATCAATTTCG-3′	This paper	N/A
shRNA for mouse MOF: 5′-CGAAA TTGATGCCTGGTATTTCTCGAGAA ATACCAGGCATCAATTTCG-3′	This paper	N/A
shRNA for mouse MOF: 5′-GCCTTC CAGTTCACTGACAAACTCGAGTTT GTCAGTGAACTGGAAGGC-3′	This paper	N/A
shRNA for mouse SIRT2: 5′-CAGTGT CAGAGTGTGGTAAAGCTCGAGCTT TACCACACTCTGACACTG-3′	This paper	N/A
sgRNA for Prdx1 Knockout in Raw 264.7 cells: 5′-AAGCGCACCATTGCTCAGGA-3′	This paper	N/A
sgRNA for Prdx1 Knockout in Raw 264.7 cells: 5′-AGCGCACCATTGCTCAGGAT-3′	This paper	N/A
sgRNA for Prdx1 Knockout in Raw 264.7 cells: 5′-TCGACAGATAACAATAAACG-3′	This paper	N/A

(*Continued on next page*)

Continued

REAGENT or RESOURCE	SOURCE	IDENTIFIER
sgRNA for Prdx1 Knockout in HEK293 cells: 5′-CACGGAGATCATTGCTTTCA-3′	This paper	N/A
sgRNA for Prdx1 Knockout in HEK293 cells: 5′-CGGAGATCATTGCTTTCAGT-3′	This paper	N/A
sgRNA for Prdx1 Knockout in HEK293 cells: 5′-TTGGTATCAGACCCGAAGCG-3′	This paper	N/A
Overlapping PCR primers for site-specific mutation on PRDX1, see Table S4	This paper	N/A
qPCR primers, see Table S5	This paper	N/A
Recombinant DNA		
pCDHblast lentiviral vector	Pegoraro et al.[96]	Addgene; Cat# 22661
Human PRDX1-expressing plasmid	Baltz et al.[97]	Addgene; Cat# 38086
pSpCas9(BB)-2A-GFP (PX458)	Ran et al.[98]	Addgene; Cat# 48138
psPAX2 plasmid	Laboratory of Prof. Didier Trono	Addgene; Cat# 12260
pMD2.G plasmid	Laboratory of Prof. Didier Trono	Addgene; Cat# 12259
pCS2+HyPer7-NES	Pak et al.[54]	Addgene; Cat# 136467
pCS2+HyPer7-NLS	Pak et al.[54]	Addgene; Cat# 136468
pCMV-HyPer7-MEM	Pak et al.[54]	Addgene; Cat# 136465
Yeast Trx and TrxR -expressing plasmids	Laboratory of Prof. Sang Won Kang	N/A
pLKO.1-puro vector	Sigma-Aldrich	Cat# SHC001
pLKO.1-puro non-mammalian shRNA control plasmid	Sigma-Aldrich	Cat# SHC002
pET28(a)	Novagen	Cat# 70777
pFastBac vector	Thermo Fisher	Cat# 10712024
Software and algorithms		
Image Lab software (v5.2)	Bio-Rad	https://www.bio-rad.com
StepOnePlus Software (v2.3)	Thermo Fisher	https://www.thermofisher.com
FlowJo software (v10)	Flowjo Software	https://www.flowjo.com/
Gen5 (v2.0)	Agilent	https://www.agilent.com
GraphPad Prism (v10)	GraphPad Software	https://www.graphpad.com
PyMOL	Schrodinger	https://pymol.org/2/
MaxQuant (v. 1.6.5.0)	Max Planck Institute of Biochemistry	https://www.maxquant.org/
Seahorse XFe 96 Wave software (v2.6)	Agilent	https://www.agilent.com

EXPERIMENTAL MODEL AND STUDY PARTICIPANT DETAILS

Generation and activation of bone marrow-derived macrophages

For generation of BMDMs, tibia and femur from 8 to 10-week-old male C57BL/6 wild-type (The Jackson Laboratory) or Myd88 KO mice[99] were isolated. Bone marrow cells were flushed out with RPMI-1640 medium and then passed through a 70 μm cell strainer. Cells were collected by centrifugation and counted. A total of 2×10^6 bone marrow cells was grown in a non-treated 10-cm dish (Corning) with RPMI-1640 medium (Gibco, 42401-018) containing 2 mM GlutaMax supplement (Gibco, 35050061) and 10% FBS (Sigma-Aldrich, F7524) supplemented with 10% L929 conditioned medium for macrophage differentiation (hereafter "macrophage medium") at 37°C in 5% CO_2. Additional macrophage medium was added on days 3 and 5. By day 6, 5–6 million BMDMs per dish were typically obtained and confirmed by flow cytometry (PE-conjugated F4/80 and APC/Cyanine7-conjugated CD11b antibodies; around 98% double-positive cells).

For activation at day 7, BMDMs (5×10^6 per 10-cm dish) were grown with media in the absence of L929 conditioned medium in a non-treated culture dish and then stimulated with TLR agonists or IL-4/IL-10 (concentration and incubation time as indicated in figure legends). For transduction, BMDMs (5×10^6 per 10-cm dish) were incubated with lentiviral particles overnight. The next day, BMDMs transduced with a shRNA plasmid were selected by incubation with 6 μg/mL puromycin for 24 h or BMDMs transduced with a PRDX1-expressing plasmid were selected by incubation with 7 μg/mL Blasticidin for 24 h. Cells at day 3 post-transduction were stimulated with 100 ng/mL of LPS for indicated time.

Cell culture

Raw264.7 cell line and HEK293 cell were acquired from BIOSS excellence cluster, Freiburg, Germany and were cultured in GlutaMAX supplemented DMEM medium (Gibco, 31966-021) with 10% fetal bovine serum (PAN-Biotech or anprotec) at 37°C in 5% CO_2. L929 mouse fibroblast cells were gifts from Laboratory of Dr. Tim Lämmermann and were cultured in GlutaMax-supplemented DMEM medium with 10% fetal bovine serum at 37°C in 5% CO_2.

Animal experiments

All animal experiments were performed in accordance with the guidelines for the use of experimental animals of German ethics laws, approved by local authorities, the Committee on Research Animal Care and the Regional Council Freiburg, and conducted under the project Akh-iTo-2 (sacrifice without pretreatment) with approval from the Max Planck Institute's welfare officer, Dr. Stefanie Kunz.

METHOD DETAILS

Generation of anti-PRDX1 K197ac antibody

The C-terminal 14 amino acid (186–199) peptide of human PRDX1 with acetylation at lysine197 (PDVQKSKEYFSKacQK) was synthesized, KLH-conjugated and used to immunize rabbits. Sera were affinity purified using an acetylated peptide column followed by a non-acetylated peptide column to obtain the final PRDX1 K197ac antibody (Genscript).

Plasmid construction

For ectopic expression of MOF, plasmids were generated as described previously.[100] Briefly, mouse wild-type or E350Q mutation of MOF was C-terminally Flag-tagged and cloned into a CMV-driven lentiviral vector (vector from Addgene, 22661). For ectopic expression of PRDX1, plasmid encoding human PRDX1 (Addgene, 38086) was cloned into same vector with an N-terminal FLAG tag. PRDX1 mutants were generated by overlapping PCR with site-specific mutated primers (Table S4). For shRNA plasmid cloning, forward and reverse complementary DNA oligonucleotides were synthesized (Sigma-Aldrich), annealed, ligated to pLKO.1-puro vector (Sigma-Aldrich, SHC001). The shRNA control contains non-targeting control for mammalian cells, which was obtained from Sigma-Aldrich (SHC002).

Production of L929 conditioned medium

L929 mouse fibroblast cells (2×10^6) were seeded in a T175 flask and supplemented with 5 mL of GlutaMax-supplemented DMEM medium on day 7. Culture supernatant was harvested on day 10 by centrifugation (3,000 rpm, 10 min), filtered through a 0.22 μm filter, aliquoted, and stored at −20°C until use.

Generation of lentiviral particles

HEK293 cells were cultured in GlutaMAX-supplemented DMEM medium with 10% fetal bovine serum (PAN-Biotech or anprotec) at 37°C in 5% CO_2. Cells (5×10^6) in a 10-cm tissue culture plate were co-transfected with 3.33 μg lentiviral plasmid, 2.5 μg psPAX2 packaging plasmid (Addgene, 12260), and 1 μg pMD2.G envelope-expressing plasmid (Addgene, 12259) using Lipofectamine 2000 reagent (Thermo Fisher). Culture supernatants were collected on days 2 and 4 and concentrated using Lenti-X concentrator (Takara).

CRISPR-Cas9-mediated gene knockout

Raw264.7 cells and HEK293 cells were cultured in GlutaMAX-supplemented DMEM medium with 10% fetal bovine serum at 37°C in 5% CO_2. Small guide RNAs (sgRNAs) targeting PRDX1 exon 3 or exon 4 in mouse (NC_000070.7; Gene ID: 18477) and human (NC_000001.11; Gene ID: 5052) gene loci were designed for CRISPR-Cas9 editing. Each sgRNA was cloned into pSpCas9(BB)-2A-GFP (PX458) plasmid (Addgene, #48138). Raw264.7 cells or HEK293 cells were transfected with plasmids using Lipofectamine 2000 and single-cell sorted into a 96-well plate using MoFlo sorter. Single cell clones were screened by immunoblotting with anti-PRDX1 antibody. *Prdx1* KO Raw264.7 and HEK293 cells were maintained in GlutaMAX-supplemented DMEM medium with 10% fetal bovine serum.

Subcellular fractionation and Western blot

For whole cell lysis, cells were lysed on ice for 20 min with RIPA buffer (150 mM NaCl, 0.5% sodium deoxycholate, 1% NP-40, 50 mM Tris-Cl, pH 7.5). Subcellular fractions (cytoplasmic, membrane, soluble nuclear, and chromatin) were isolated simultaneously using the subcellular protein fractionation kit for cultured cells (Thermo Fisher). Lysis buffers were supplemented with 20 mM sodium butyrate, 10 mM nicotinamide, protease inhibitors (Roche), and PhosSTOP (Roche). Lysates were quantified using the Bradford assay (Bio-Rad), diluted with 6× sample buffer, boiled at 95°C for 5 min, and resolved on a 12% Bis-Tris gel. Proteins were transferred onto PVDF membranes (Amersham), probed with primary antibodies followed by HRP-conjugated secondary antibodies. Immunodetection was performed using Lumi-Light Western Blotting Substrate (Roche). Images were captured with ChemiDoc XRS+ (Bio-Rad), and band intensities were quantified using Image Lab software (v5.2, Bio-Rad).

Reverse transcription followed by quantitative PCR

Cells were lysed in TRIzol reagent (Thermo Fisher) to collect total RNA, which was further extracted using Direct-zol RNA Miniprep Plus Kits (Zymo Research) according to the manufacturer's instructions. cDNA was synthesized using the GoScript Reverse Transcription kit (Promega). For quantitative PCR (qPCR), diluted cDNA was amplified with SYBR Green dye (Roche) on a StepOnePlus Real-Time PCR System (Thermo Fisher). Relative RNA expression differences among samples were determined using the comparative C_T ($\Delta\Delta C_T$) method in StepOnePlus Software v2.3. Briefly, C_T values were first normalized to that of housekeeping gene HPRT in the same sample (ΔC_T) and then differences of C_T values between each treated and control group ($\Delta\Delta C_T$) were used to calculate the fold changes within each sample using the formula $2^{-\Delta\Delta C_T}$. Each qPCR experiment included three technical replicates per biological sample. Primers used are listed in Table S5.

RNA sequencing analysis

BMDMs were transduced overnight with lentiviral particles carrying shRNA against MOF (shMOF) or non-targeting control (shCTRL) plasmids, followed by selection with 6 μg/mL puromycin. At day 3 post-transduction, cells were either stimulated with LPS for 3 h or left unstimulated. Total RNAs from 3 independent samples were extracted using Direct-zol RNA Miniprep Plus Kits (Zymo Research), and their concentration were quantified with Qubit 2.0 (Thermo Fisher). Paired-end libraries (100 bp length) were prepared using Illumina TruSeq Stranded mRNA Prep, Ligation (Illumina, 20040534), and sequenced on a NovaSeq 6000 (Illumina) at the Deep Sequencing Facility of the Max Planck Institute for Immunobiology and Epigenetics.

Raw sequencing data were processed using the snakePipes mRNA-seq pipeline (v2.5.0).[101] Adapters were trimmed with cutadapt (v2.8) using parameters '-q 20 –trim-n'. Trimmed reads were aligned to the mm10 genome using STAR (v2.7.4).[102] The aligned reads were counted using Gencode GTF (m9) via featureCounts (v2.0.0)[103] The gene-level counts obtained from featureCounts were used for differential expression analysis via DESeq2 (v1.26.0).[104] Differential expression analysis was performed using DESeq2 (v1.26.0),[104] with genes considered differentially expressed at a q-value cutoff of 0.05. Gene Ontology (GO) enrichment analysis of differentially expressed genes was conducted using ClusterProfile (v3.17.4).[105] Normalized counts from DESeq2 were used for gene expression comparisons across samples. MA plots, dot plots, and heatmaps depicting gene expression changes were generated using ggplot2 (v3.3.2) and pheatmap (v1.0.12) in R (v4.1.3).

Recombinant protein expression and purification

His-tagged wild-type or mutant human PRDX1 was cloned into the pET28(a) vector (Novagen, 70777) and transformed into Rosetta 2 (DE3) *E. coli*. A single colony was grown overnight in 10 mL LB broth containing 50 mg/mL kanamycin and 30 mg/mL chloramphenicol. The culture was expanded to 500 mL in a 2 L shaker flask, and grown at 37°C until an OD600 of 0.6–0.8 was reached. Protein expression was induced with 1 mM IPTG at 30°C for 4 h. Cells were harvested by centrifugation (6,000 rpm, 15 min, 4°C), resuspended in ice-cold lysis buffer (50 mM Tris-HCl, pH 7.5, 150 mM NaCl, 2 mM imidazole, protease inhibitors), and sonicated. The lysate was centrifuged (20,000 rpm, 20 min, 4°C), and the supernatant was incubated with Ni-NTA beads (Qiagen) for 2 h at 4°C with gentle rotation. The beads were washed sequentially with three buffers: wash buffer 1 (10 mM imidazole), wash buffer 2 (25 mM imidazole), and wash buffer 3 (40 mM imidazole), which are all containing 50 mM Tris-HCl, pH 7.5, 150 mM NaCl, and protease inhibitors. Protein was eluted with elution buffer (50 mM Tris-HCl, pH 7.5, 500 mM NaCl, 200 mM imidazole, protease inhibitors). After concentration (Amicon, Millipore) and centrifugation (20,000 rpm, 10 min), gel filtration was performed using HPLC with a Superdex 200 10/300 GL column (Cytiva) equilibrated with 20 mM Tris, 150 mM NaCl, pH 7.5. PRDX1 monomers were collected, concentrated, quantified by Bradford assay, flash-frozen in liquid nitrogen and stored at −80°C.

The pET17b-yTrx and yTrxR plasmids,[52] gifts from Prof. Sang Won Kang (Ewha Womans University, Seoul, South Korea), were used to transform *E. coli* BL21(DE3). A 500 mL expression culture was initiated from 50 mL of a single cell clone culture, and protein expression was induced with 1 mM IPTG at 30°C for 4 h. Cells were harvested by centrifugation (6,000 rpm, 15 min, 4°C), resuspended in ice-cold lysis buffer (20 mM Tris-HCl, pH 7.5, 10 mM NaCl, 1 mM EDTA, 5 mM DTT, protease inhibitors), and sonicated. The lysate was centrifuged (20,000 rpm, 30 min), and the supernatant treated with salt-active nuclease (Serva) on ice for 10 min, followed by another centrifugation (20,000 rpm, 20 min).

For yTrxR purification, the supernatant was loaded onto a DEAE Sepharose column (Cytiva), washed with buffer A (20 mM Tris–HCl pH 7.5, 1 mM EDTA), and eluted with a step gradient of 0–500 mM NaCl. Fractions containing yTrxR were collected, concentrated using a 10 kDa Amicon and dialyzed against buffer B (20 mM HEPES-NaOH, pH 7.0, 1 mM EDTA) using a 3.5 kDa dialysis cassettes (Thermo Fisher). Following dialysis, an equal volume of 2M ammonium sulfate dissolved in buffer B was added to equilibrate the post-dialyzed proteins. The yTrxR was further purified on a Phenyl Sepharose column (Cytiva) using a reverse gradient of 1-0 M ammonium sulfate in buffer B. Pure yTrxR fractions were pooled, concentrated, dialyzed against assay buffer (50 mM HEPES-NaOH, pH 7.0, 1 mM EDTA), quantified by Bradford assay, flash-frozen in liquid nitrogen and stored at −80°C.

For yTrx purification, the supernatant was similarly loaded onto a DEAE Sepharose column, washed with buffer A, and eluted with a step gradient of 0–500 mM NaCl. Fractions containing yTrx were concentrated using a 3 kDa Amicon and purified on a Superdex 200 10/300 GL column equilibrated with 20 mM Tris, 150 mM NaCl, pH 7.5. Pure yTrx fractions were pooled, concentrated, quantified by Bradford assay, flash-frozen in liquid nitrogen and stored at −80°C.

For cloning, expression and purification of $MOF_{1\text{-}458}$ in Sf21 cells, the Bac-to-Bac expression system (Thermo Fisher) was used to express N-terminally tagged HA-3XFLAG-$MOF_{1\text{-}458}$ in Sf21 cells. The human MOF gene was cloned into the pFastBac vector.

Bacmids were generated in DH10Bac *E. coli*, and Sf21 cells were transfected with 0.5–1 μg bacmid-DNA using Cellfectin II (Thermo Fisher). Virus stocks were harvested after 4 days, and cell pellets for protein purification were collected after 2 days. The cell pellet was lysed in buffer (25 mM Tris, 150 mM NaCl, 10% glycerol, protease inhibitors, pH 7.4) using dounce homogenization (20 cycles). After centrifugation (40,000 g, 4°C, 30 min), the supernatant was incubated with anti-FLAG M2 agarose beads (Sigma-Aldrich) for 1.5 h at 4°C with gentle rotation. The beads were washed four times with lysis buffer and centrifuged (5 min, 1,000 g, 4°C). Elution was performed by incubating the beads with lysis buffer containing 3XFLAG-peptide (250 μg/mL) for 1 h at 4°C with gentle rotation. The eluent was collected and further purified using a Superdex S200 10/300 gel filtration column (Cytiva) in buffer (25 mM Tris, 150 mM NaCl, 10% glycerol, pH 7.4). Fractions containing MOF were pooled, concentrated, flash-frozen in liquid nitrogen, and stored at −80°C. SDS-PAGE followed by InstantBlue (Expedition) was used to monitor all purification steps.

In vitro peroxidase assay

Purified 0.5 μM hPrdx1, 5 μM yTrx, 0.5 μM yTrxR, and 200 μM NADPH were mixed in 180 μL per reaction with assay buffer (50mM Hepes-NaOH pH 7.0, 1mM EDTA). The 180 μL of pre-cocktail was transferred into each well in a clear flat-bottom black well 96-well plate (FALCON, 353219) and the reaction was initiated by adding final concentration of 10 μM H_2O_2 to 180 μL pre-cocktail. The NADPH oxidation was monitored for 15 min by absorbance at 340 nm at 30°C (measurement every 20 s) via VICTOR Nivo Multimode Plate Reader (PerkinElmer).

In vitro HAT assay

In vitro acetylation of PRDX1 was performed using 2 μM of recombinant human PRDX1 protein incubated at 30°C for 2 h at 300 rpm with 0.2 μM of recombinant human MOF and 20 μM of acetyl-CoA (Sigma-Aldrich) in a buffer containing 10 mM Tris-HCl pH8.0, 150 mM NaCl, and 1 mM DTT (30 μL final volume). The reaction mixture was separated on a Tris-glycine gel, followed by immunoblotting with an anti-acetyllysine or anti-PRDX1 K197ac antibody.

Mass spectrometry

For identifying acetylation sites, *in vitro* HAT reactions were mixed with Laemmli buffer adjusted to 10.5 mM TCEP (pH7.0), heated for 10 min (70°C), followed by SDS-PAGE (16% Novex, Thermo Fisher; colloidal Coomassie, Expedeon). In-gel propionylation followed a published method.[106] In-gel digestion with trypsin (Promega) and peptide clean-up were as previously described.[107] Nano-scale LC-MS analysis was performed on a Q Exactive mass spectrometer as previously described[108] with modifications below. Samples were injected twice employing a "60 min" and "120 min" nLC-MS method, respectively. The 60 min method: gradient: 10% for 5 min, 40% for 40 min, 80% for 4 min (%B buffer; 250 nL/min flow rate), followed by a wash-out step: 80% for 5 min, inverse gradient from 80% to 0% for 1 min, and re-equilibration at 2% B buffer for 5 min (flow rate: 450 nL/min). The 120 min method: gradient: 5% for 5 min, 30% for 90 min, 40% for 10 min, 80% for 2 min (%B buffer; 300 nL/min flow rate), followed by a wash out: 80% for 5 min, inverse gradient from 80% to 2% for 2 min, and re-equilibration at 2% B buffer for 5 min (flow rate: 500 nL/min). All measurements were carried out in DDA mode employing the "sensitive method". Data were analyzed using MaxQuant (v. 1.6.5.0) employing standard parameters for peptide and final protein identification role-up (both at 1%FDR). MS raw data were searched simultaneously with the target-decoy standard settings against the Uniprot Homo sapiens database (Uniprot_reviewed+Trembl including canonical isoforms; August 2019) concatenated with an in-house curated FASTA file containing commonly observed contaminant proteins. Cysteine carbamidomethylation was set as a fixed modification and N-terminal acetylation, lysine acetylation, deamidation (NQ) and methionine oxidation as variable modifications. For in-gel propionylated samples lysine propionylation was added. For identification of post-translational modifications, site FDR was set to 5%. Mass spectrometry raw data were analyzed similarly as previously described[106] using Peaks Studio version X (Bioinformatics Solution Inc.) enabling the 'inchorus' mode including an optional Mascot 2.2 database search using the decoy-fusion database search strategy (1% peptide FDR). Parameter settings for PTM searches were set as described above. Maximum (allowed) variable PTMs per peptide were set to four.

Measurement of extracellular acidification rates (ECAR)

To examine glycolysis rates, the Seahorse Glycolysis Stress Assay was performed using the XF96 Extracellular Flux Analyzer (Agilent). Transduced or treated BMDMs were plated at 50,000 cells/well on attachment factor-coated Seahorse XF Cell Culture Microplates (Agilent) with macrophage medium and incubated overnight. The next day, cells were treated with or without 100 ng/mL LPS in macrophage medium without L929 conditioned medium for 3 h. Cells were then washed with assay medium (Agilent) and replaced with 180 μL of assay medium without glucose. Plates were incubated at 37°C in a non-CO_2 incubator for 60 min to degas, while ensuring cells were undisturbed using Bright Field imaging.

During the assay, glucose (10 mM), oligomycin (1 μM), and 2-DG (50 mM) were sequentially added to ports A, B, and C, respectively. Hoechst dye (Thermo Fisher) was added to port C for cell counting via BioTek Cytation imager post-assay. Four baseline measurements were taken before adding any compounds, followed by measurements after each sequential addition. Glycolysis was calculated by subtracting the last ECAR measurement before glucose injection from the maximum ECAR value prior to oligomycin injection. Glycolytic capacity was calculated by subtracting the last ECAR measurement before glucose injection from the maximum ECAR value post-oligomycin injection. Data were analyzed using Seahorse XFe 96 Wave software, and ECAR values were normalized to cell numbers, reported as absolute rates (mpH/min/1000 cells).

Peroxy Orange 1 staining

Intracellular hydrogen peroxide levels were assessed using Peroxy Orange 1 (PO-1) staining (Tocris Bioscience). Transduced BMDMs (1.2×10^6 cells/well) or PRDX1-complemented *Prdx1* KO Raw264.7 cells (2×10^6 cells/well) were seeded in 6-well plates. The next day, cells were incubated with 10 μM PO-1 for 20 min and then stimulated with 100 ng/mL LPS for 3 h at 37°C. Cells were washed with PBS, detached using 20 mM EDTA in PBS or Trypsin, and resuspended in PBS with 1 μg/mL DAPI for live/dead cell analysis. Stained cells were analyzed for oxidized PO-1 fluorescence (ex. 543 nm/em. 647 nm) and DAPI (ex. 358 nm/em. 461 nm) using a Fortessa III flow cytometer (BD), acquiring at least 10,000 events per sample. Mean fluorescence intensity (MFI) of oxidized PO-1 was calculated using FlowJo software (v10), and fold changes were normalized to the control by MFI.

Enzyme-linked immunosorbent assay (ELISA)

Transduced or treated BMDMs (1.2×10^6 cells/well) or PRDX1-complemented *Prdx1* KO Raw264.7 cells (2×10^6 cells/well) were seeded in 6-well plates and stimulated with 100 ng/mL LPS for 3 h in 1 mL of medium. Culture supernatants were collected by centrifugation at 500 × g for 5 min. Mouse IL-6 ELISA assays (BioLegend, 431307) were conducted according to the manufacturer's protocol. Absorbance at 450 nm was measured using a Bio-tek Synergy4 Multimode Plate Reader, and results were analyzed with Gen5 2.0 software.

HyPer7 measurements

HyPer7 sequences in plasmids pCS2+HyPer7-NES (cytoplasm, Addgene, 136467), pCS2+HyPer7-NLS (nucleus, Addgene, 136468), and pCMV-HyPer7-MEM (plasma membrane, Addgene, 136465), were cloned into a CMV-driven lentiviral vector. Lentiviral particles carrying Hyper7 plasmids were generated. HEK293 *Prdx1* KO cells were co-transduced with PRDX1-and Hyper7-expressing plasmids at 1:1 ratio. After a 24-h infection, cells were selected with 16 μg/mL Blasticidin for 3–6 days. Subsequently, cells (5×10^5/12 well) were treated with 50 μM hydrogen peroxide or left untreated for 3 h. Cells were then trypsinized, resuspended and analyzed for fluorescence - reduced Hyper7 (ex. 405 nm/em. 530 nm) and oxidized Hyper7 (ex. 488 nm/em. 530 nm) – using Fortessa III flow cytometer (BD). At least 10,000 events per sample were acquired. The ratio of oxidized to reduced Hyper7 fluorescence intensity per cell was calculated using FlowJo software (v10, Flowjo Software). Geometric means of the ratios per sample were presented.

Immunofluorescence

To confirm HyPer7 localization, HyPer7-expressing cells (1×10^5/well) were seeded onto ibi-treated μ-Slide 8 Well chambers (ibidi). For Alexa Fluor 555 Wheat Germ Agglutinin (WGA) (Thermo Fisher) staining, cells were incubated with 1 μg/mL WGA in PBS at 37°C for 10 min. Cells were then fixed using 4% methanol-free formaldehyde (Thermo Fisher) at RT for 10 min, permeabilized with 0.2% Triton X-100 in PBS at RT for 10 min, and blocked with 2% BSA in PBS for 1 h. Cells were incubated with mouse anti-GFP primary antibody (Roche) at 4°C overnight. The next day, cells were washed with PBS and incubated with Alexa Fluor 488-conjugated goat anti-mouse secondary antibody (Thermo Fisher) at RT for 1 h. For Alexa Fluor 647 Phalloidin (Cell Signaling Technology) staining, antibody-stained cells were incubated with a 1:20 dilution of Alexa Fluor 647 Phalloidin in PBS at RT for 15 min. Samples were mounted using DAPI-containing medium (Vector Laboratories) and imaged with a Spinning Disc microscope.

Redox state assessment of PRDX1

Sample preparation was followed as described previously.[109] Briefly, Flag-tagged PRDX1-complemented HEK293 Prdx1 KO cells were either treated with 50 μM H_2O_2 for indicated time or left untreated. After H_2O_2 treatments, cells were washed with 1X PBS and incubated with 100 mM N-ethylmaleimide (Sigma) in PBS for 10 min at room temperature to alkylate free cysteine residues.

For PRDX1 dimerization, cells were lysed in a buffer containing 40 mM HEPES, 50 mM NaCl, 1 mM EGTA, 1% CHAPS, Complete protease inhibitors (Roche), pH 7.4, and 10 mg/mL catalase (Sigma), along with 100 mM N-ethylmaleimide (NEM). Lysates were diluted in a nonreducing sample buffer (62.5 mM Tris-HCl, pH 7.0, 10% glycerol, 1.5% SDS, and 0.025% bromophenol blue) and resolved on a 12% Bis-Tris SDS-PAGE followed by Western blotting. Band intensities of PRDX1 dimer and monomer were quantified using Image Lab software (v5.2, Bio-Rad), and ratios (monomer/dimer) relative to control samples were calculated.

For PRDX1 hyperoxidation, NEM-treated cells were harvested and lysed in a buffer with 50 mM Tris, 150 mM NaCl, 1% Triton X-100, 0.1% SDS, pH 7.4. After protein quantification, 1000 μg of total lysates was incubated with 5 μL of anti-Flag M2 antibody overnight at 4°C with rotation and then incubated with 30 μL of Protein A/G Magnetic beads (Thermo Fisher) for another 2 h. Subsequently, the beads were washed with 0.05% TBST three times. Proteins were eluted in SDS-PAGE reducing sample buffer in a 95°C heating block for 10 min and then magnetically separated from the beads for Western blotting.

QUANTIFICATION AND STATISTICAL ANALYSIS

Data were analyzed using GraphPad Prism version 10.0. All data represent mean ± s.e.m. of the corresponding number of samples, except for Hyper7 ratio data, which represent geometric mean ± s.e.m. All experiments in this study were repeated at least three times. The number of corresponding biological samples and statistical hypothesis tests are detailed in the figure legends. Briefly, statistical analyses included two-tailed unpaired t-tests (Figures 1F–1I, 3I, 5E, 5F, 5H, 5I, 6O, S3K, and S5A), one-way ANOVA (Figures 2C, 2E, 2G, 2I, 2K, 2M, 5B, 5G, 6G, 6H, 6L, 6M, 6P, S2B, and S2D), two-way ANOVA (Figures 3B, 3C, 3F, 3H, 3K–3M, 4J, 6C, 6E, 6F, 6I, 6J, 6N, S3F, S3I, and S6A), and mixed effect analysis (Figure S5C). *p*p-values <0.05 were considered statistically significant and are reported as exact values in the figures, while *p*p-values >0.05 were considered not statistically significant and are denoted as "ns".